

## KINEMATICS OF SPIRAL-ARM STREAMING IN M51

RAHUL SHETTY, STUART N. VOGEL, EVE C. OSTRIKER, AND PETER J. TEUBEN  
Department of Astronomy, University of Maryland, College Park, MD 20742-2421; shetty@astro.umd.edu,  
vogel@astro.umd.edu, ostriker@astro.umd.edu, teuben@astro.umd.edu

*Received 2007 January 9; accepted 2007 May 21*

### ABSTRACT

We use CO and H $\alpha$  velocity fields to study the gas kinematics in the spiral arms and interarms of M51 (NGC 5194), and fit the 2D velocity field to estimate the radial and tangential velocity components as a function of spiral phase (arm distance). We find large radial and tangential streaming velocities, which are qualitatively consistent with the predictions of density wave theory and support the existence of shocks. The streaming motions are complex, varying significantly across the galaxy as well as along and between arms. Aberrations in the velocity field indicate that the disk is not coplanar, perhaps as far in as 20'' (800 pc) from the center. Velocity profile fits from CO and H $\alpha$  are typically similar, suggesting that most of the H $\alpha$  emission originates from regions of recent star formation. We also explore vortensity and mass conservation conditions. Vortensity conservation, which does not require a steady state, is empirically verified. The velocity and density profiles show large and varying mass fluxes, which are inconsistent with a steady flow for a single dominant global spiral mode. We thus conclude that the spiral arms cannot be in a quasi-steady state in any rotating frame, and/or that out-of-plane motions may be significant.

*Subject headings:* galaxies: individual (M51) — galaxies: kinematics and dynamics — galaxies: spiral

### 1. INTRODUCTION

Spiral arms are the dominant morphological features of most disk galaxies. From a theoretical perspective, two frameworks have been proposed to describe the nature of the spiral arms: one is that the spiral arms are generally long lasting or slowly evolving, and the other is that the arms are transient features (e.g., Toomre & Toomre 1972). Observational studies have yet to show definitively whether the arms are evolving or long lived, although it has been over 40 years since the landmark paper by Lin & Shu (1964) suggesting that spiral structure in galaxies is a long-lived phenomenon—the quasi-stationary spiral structure (QSSS) hypothesis (Lindblad 1963). In the QSSS depiction, although material passes in and out of the arms, the slowly evolving global pattern rotates with a single angular speed that results from the excitation of global modes. The spiral arms are formed from self-excited and self-regulated standing density waves (Bertin et al. 1989a, 1989b; Bertin & Lin 1996).

However, interaction between a disk galaxy and a companion is another explanation for the presence of spiral arms. In such a framework, the arms are transient features that are generated by the tidal interaction (e.g., Toomre & Toomre 1972). Any spiral arms existing before the encounter are overwhelmed by the tidal driving (Salo & Laurikainen 2000).

Regardless of the origin of the stellar arms, gas in the disk will respond strongly to the gravitational perturbations those arms impose. Numerical studies have indicated that shocks can develop if the relative speed between the spiral perturbation and the gas is large (Roberts 1969; Shu et al. 1973; Woodward 1975). The presence of dust lanes in the spiral arms and the enhancement in ionized emission downstream, indicating regions of star formation, is attributed to this shock scenario. Such shocks are also thought to be the cause of the well-defined molecular arms seen in many grand-design galaxies, including M51. Numerical and analytical studies have provided predictions for the velocity and density profiles of the matter affected by the spiral gravitational perturbation (e.g., Lubow et al. 1986; Kim & Ostriker 2002; Gittins & Clarke 2004).

There have been numerous observational studies addressing the nature of spiral structure that have focused on the gaseous components. Visser (1980) showed that steady state density wave models fit the H I kinematics of M81 quite well. Lowe et al. (1994) used the modal theory of density waves to describe the spiral pattern in M81. Both Rand (1993) and Aalto et al. (1999) used observed molecular velocities along 1D cuts on the major and minor axes of the grand-design spiral M51, and found qualitative agreement with the density wave models of Roberts & Stewart (1987). Kuno & Nakai (1997) fitted observed CO velocities from single-dish observations to obtain gas streamlines. The smooth shape of the velocity profiles led them to conclude that galactic shocks do not exist in M51. However, the study by Aalto et al. (1999) using higher resolution interferometric data found steeper velocity gradients, supporting the presence of shocks.

Yet, other observational studies have suggested that the arms are not long lived. In fact, the classic kinematic study of M51, that of Tully (1974), found evidence for a transient pattern in the outer disk due to the interaction with its companion, but that a steady state is probably appropriate for the inner arms. Elmegreen et al. (1989) and Vogel et al. (1993) also suggested the presence of multiple pattern speeds. Henry et al. (2003) argued that the spiral pattern may be a superposition of an  $m = 2$  mode and a weaker  $m = 3$  mode, suggesting a transient pattern for the arms of M51.

This paper presents a detailed study of the gaseous velocity structure associated with the spiral pattern in M51. In a future paper, we will discuss and compare the spiral pattern in different tracers. Here we use the CO and H $\alpha$  velocities to map the 2D velocity field in M51.

Our study makes use of the full 2D velocity field in M51 from interferometric CO and Fabry-Perot H $\alpha$  observations, rather than just major- and minor-axis cuts. Noting that variations in the observed velocity field are mainly associated with the spiral arms, we fit the observed velocity field to obtain the radial and tangential components as a function of arm phase (i.e., distance perpendicular to the arm). We then analyze whether the fitted velocity field and density maps are consistent with the predictions of steady state theory.

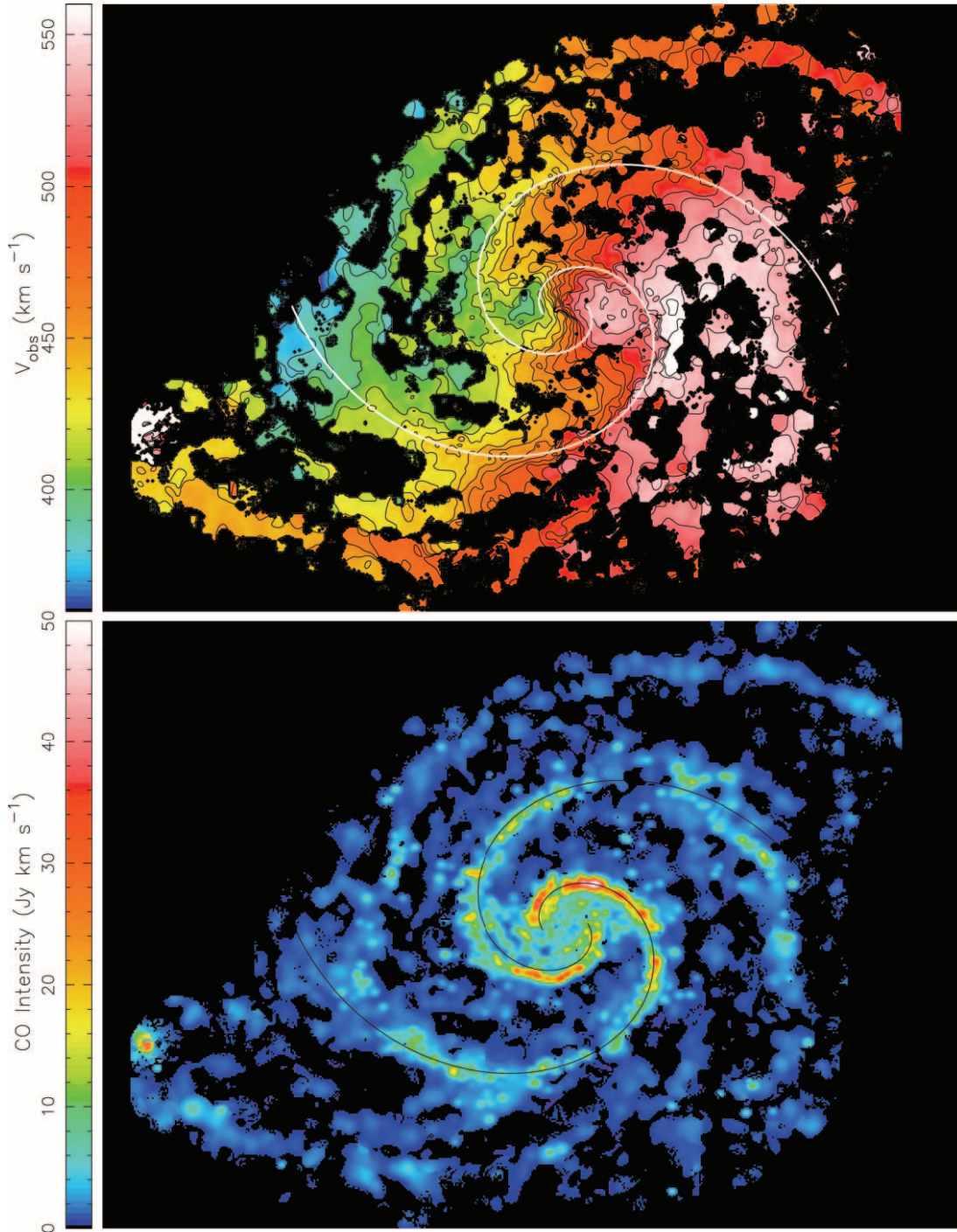


FIG. 1.—CO(1–0) velocity-integrated intensity (*bottom*) and velocity (*top*) maps of M51. Velocity contours increment by  $10 \text{ km s}^{-1}$ , between 360 and  $560 \text{ km s}^{-1}$ . Overlaid lines are logarithmic spirals with a pitch angle of  $21.1^\circ$ , separated by  $180^\circ$ .

In the next section we briefly describe our CO and  $\text{H}\alpha$  observations. In § 3 we describe the method we employ to estimate the radial and tangential velocity components throughout the disk. Since our method is sensitive to the assumed values of the systematic velocity, major-axis position angle, and disk inclination with respect to the sky, in § 4 we present results from our effort to constrain these parameters and describe how errors could affect the fitting results. In § 5 we present and discuss the fitted profiles of radial and tangential velocities for a range of radii. We then use the velocity and density profiles to empirically test conser-

vation of vortensity in § 6.1. Next, in § 6.2 we examine whether (quasi) steady state mass conservation is applicable, as would be necessary for a QSSS description. Finally, in § 7 we summarize our conclusions.

## 2. OBSERVATIONS

The CO and  $\text{H}\alpha$  intensity and velocity maps are shown in Figures 1 and 2, respectively. The CO( $J = 1-0$ ) data for M51 were obtained in part from BIMA SONG (Survey of Nearby Galaxies). The observations and data reduction are described in

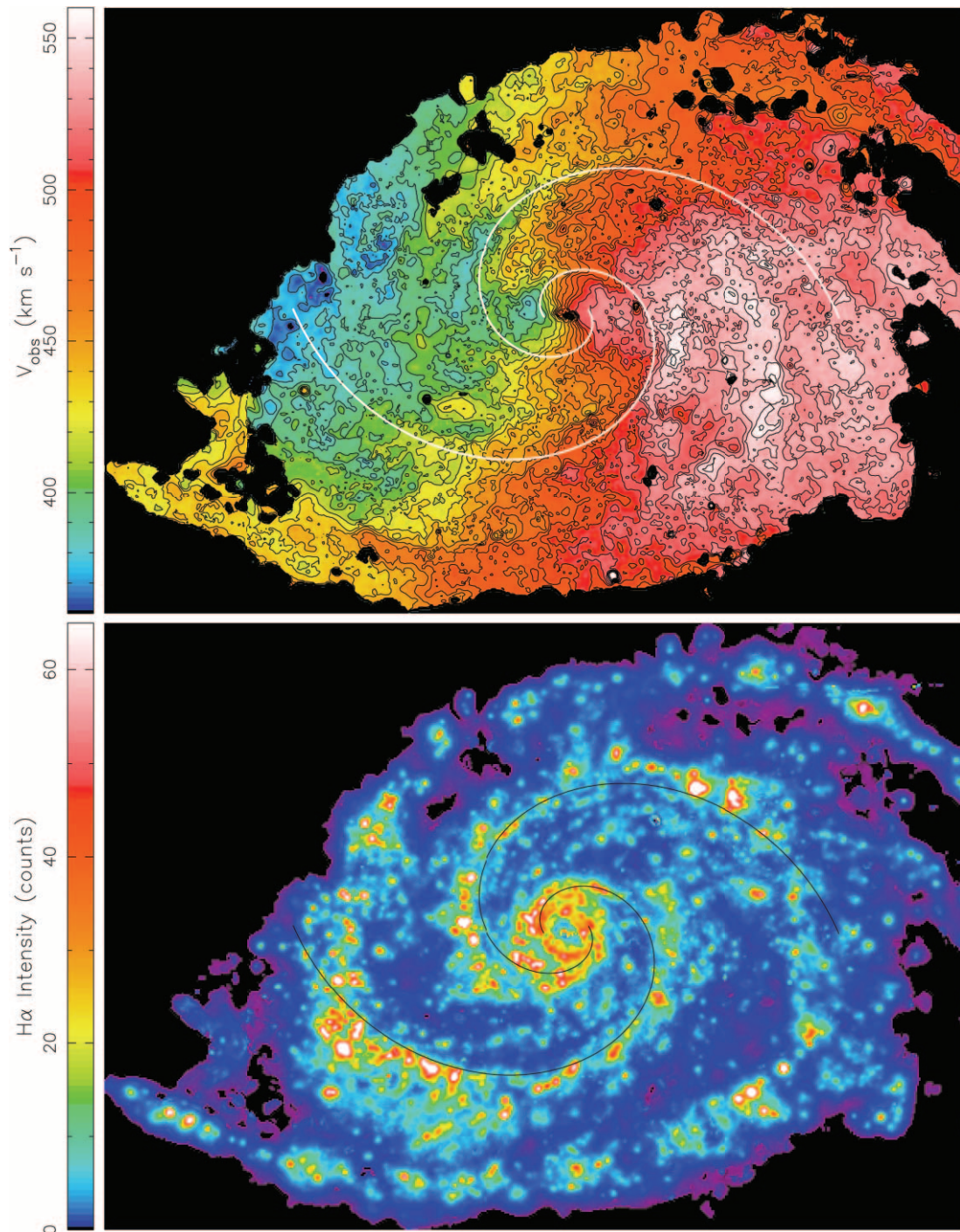


FIG. 2.— $H\alpha$  velocity-integrated intensity (*bottom*) and velocity (*top*) map of M51. The overlaid spirals, as well as the velocity contours, are as described in Fig. 1.

Regan et al. (2001) and Helfer et al. (2003). The SONG map is based on 26 pointings and has an angular resolution of  $5.8'' \times 5.1''$ . Later, we obtained data for 34 additional pointings, so that the spiral arms were mapped as far as the companion galaxy to the north and to a similar distance along the spiral arm to the south. In addition, inner fields were mapped in a higher resolution array (B array), yielding higher angular resolution. The newer data were reduced using the same procedures as described in Helfer et al. (2003) for BIMA SONG. Together the data sets cover 60 pointings. The maps used for this paper have variable resolution, reaching as high as  $4''$  in the inner spiral arms but degrading to  $6''$ – $13''$  in the interarms and in the outer arms.

$H\alpha$  data were obtained with the Maryland-Caltech Palomar Fabry-Perot, which covered the optical disk at an angular resolution of  $2''$  and a velocity resolution of  $25 \text{ km s}^{-1}$ . The observations and reduction are described in Gruendl (1996) and also Vogel et al. (1993). Both CO and  $H\alpha$  intensity maps are obtained by fitting Gaussian profiles to the spectrum at each location. The velocity maps indicate the velocity of the peak of the fit Gaussian intensity.

Also shown in Figures 1 and 2 are two lines tracing logarithmic spirals. The bright CO arm is well represented by a logarithmic spiral with a pitch angle of  $21.1^\circ$ . The weaker arm also generally follows a logarithmic spiral, although, as will be discussed, a

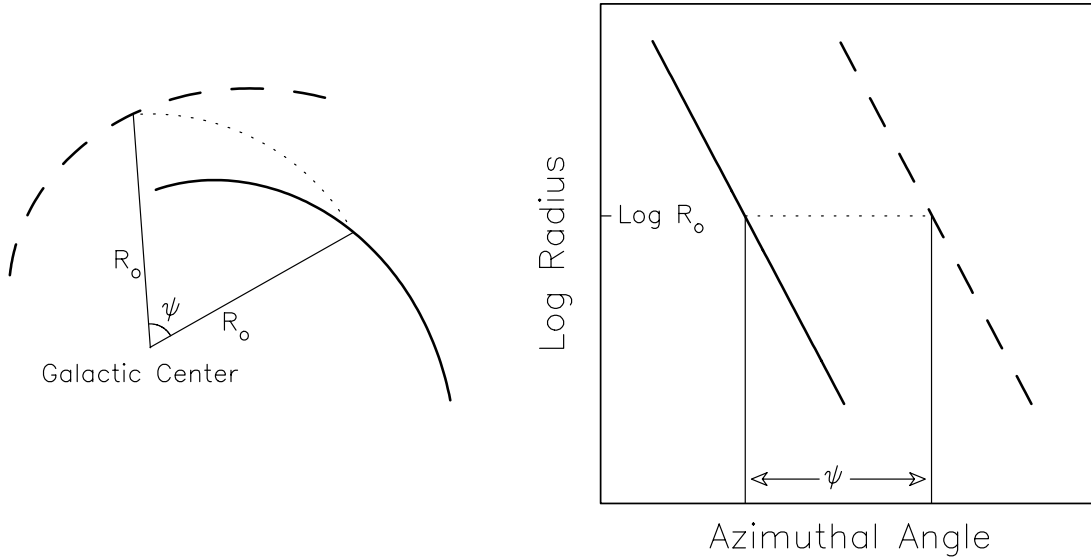


FIG. 3.—Geometry depicting the spiral-arm phase  $\psi$ . The diagram on the left is the geometry in the plane of the galaxy. The phase,  $\psi$ , represents the angular displacement between two locations with equal galactocentric radius  $R_0$  for two congruent spiral segments. The diagram on the right is the logarithmic polar projection of the geometry on the left, showing the corresponding spiral segments.

number of its arm segments either lead or lag the depicted line. The logarithmic spirals will be discussed extensively in the following sections.

### 3. ESTIMATION OF SPIRAL STREAMING VELOCITIES

The observed line-of-sight velocity  $V_{\text{obs}}$  can be decomposed as a sum of terms involving the systematic velocity  $V_{\text{sys}}$ , the radial velocity  $v_R$ , and the tangential velocity  $v_\theta$ :

$$V_{\text{obs}}(R, \theta) = V_{\text{sys}} + [v_R(R, \theta) \sin(\theta - \theta_{\text{MA}}) + v_\theta(R, \theta) \cos(\theta - \theta_{\text{MA}})] \sin i, \quad (1)$$

where  $R$  and  $\theta$  are the galactocentric radius and azimuthal angle, and  $\theta_{\text{MA}}$  and  $i$  are the position angle of the major axis and inclination of the galaxy, respectively. This equation does not include a velocity component perpendicular to the disk. The exclusion of the vertical velocity component is reasonable since studies of face-on grand-design spirals indicate that the  $z$ -component of velocity is less than  $5 \text{ km s}^{-1}$  (van der Kruit & Shostak 1982), provided the disk has no significant warp (we return to this issue in § 4.2).

Inspection of the velocity maps indicates that the isovelocity contours near the spiral arms tend to run parallel to the arms. For a disk in pure circular rotation and with a flat rotation curve, on the other hand, the isovelocity contours of the projected velocity field are purely radial. It is evident that the velocity field of M51 is significantly different from this sort of simple “spider diagram,” due to the nonaxisymmetric perturbations associated with spiral streaming. Clearly,  $v_R$  and  $v_\theta$  vary with azimuth.

Previous estimates of streaming velocities have used observed velocities near the major axis (where the projections of  $v_R$  vanish) to estimate  $v_\theta$ , and velocities near the minor axis (where the projections of  $v_\theta$  vanish) to estimate  $v_R$  (e.g., Rand 1993). However, much of the CO gas is organized into GMCs (giant molecular clouds) and larger complexes known as GMAs (giant molecular associations; Vogel et al. 1988). Further, Aalto et al. (1999) have found that the streaming velocities of M51 GMAs in the same spiral arm have a significant dispersion. Observations along a single cut, e.g., the major axis, sample discrete GMCs and therefore may give a misleading estimate of the streaming velocities.

As an alternative, an approach that fits a streaming profile to all the observed velocities in an annulus as a function of distance from the arm peak may better characterize the streaming velocities. Also, the gas surface density distribution varies significantly at any distance from the peak (i.e., the gas is clumpy), and so averaging parallel to the arm may better characterize the variation in gas surface density as a function of arm distance.

Typically, 2D fits to a galaxy velocity field assume that  $v_R$  and  $v_\theta$  are constant along rings (e.g., the tilted ring analysis described in Begeman 1989). By contrast, as mentioned earlier,  $v_R$  and  $v_\theta$  do vary with azimuth, and indeed inspection of Figures 1 and 2 indicates that the primary variations are due to the flow through the spiral arms rather than variations with galactocentric radius. As in most galaxies, the rotation curve of M51 is relatively flat; the radial variations that do occur are associated with spiral-arm streaming. Thus, we are motivated to assume that radial variations of azimuthally averaged quantities are negligible (at least over relatively limited radial ranges) and that  $v_R$  and  $v_\theta$  vary primarily with spiral-arm phase  $\psi$ . The left panel of Figure 3 shows the relevant geometry depicting the spiral-arm phase. Our assumption is that  $v_R$  and  $v_\theta$  are constant along narrow spiral arcs, such as the segments in Figure 3, that are congruent to the spiral arms. Thus, we rewrite equation (1) (for a limited range of radii) as

$$V_{\text{obs}} = V_{\text{sys}} + [v_R(\psi) \sin(\theta - \theta_{\text{MA}}) + v_\theta(\psi) \cos(\theta - \theta_{\text{MA}})] \sin i. \quad (2)$$

In order to simplify the process of identifying regions of constant arm phase, we adopt a coordinate system in which the spiral arms are straight. Elmegreen et al. (1989) show that the spiral arms of M51 appear as straight line segments in a  $(\theta, \log R)$ , or logarithmic polar, coordinate system. The right panel of Figure 3 shows the logarithmic polar diagram corresponding to the features in the left panel. Figure 4 shows the CO intensity and velocity maps of M51 in log-polar coordinates, and Figure 5 shows the corresponding  $H\alpha$  maps.

The sky images in Figures 1 and 2 are first deprojected before being transformed into a  $(\theta, \log R)$  coordinate system. In order to deproject the sky view of a galaxy, the center position, position

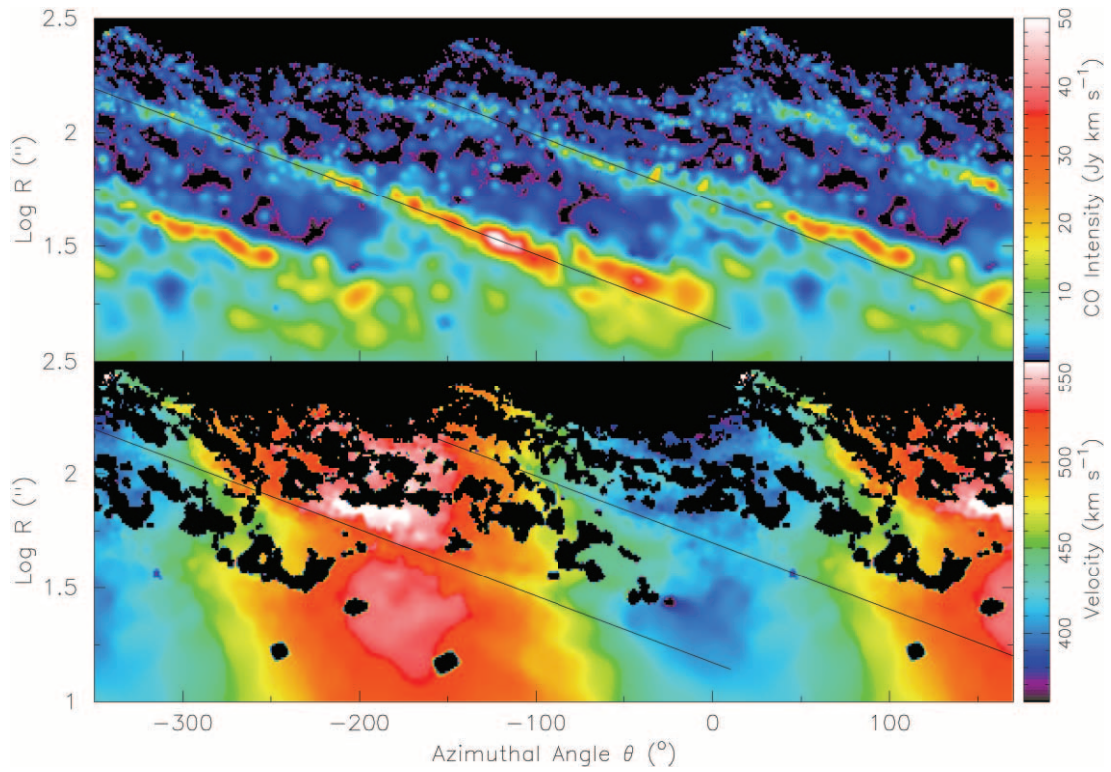


FIG. 4.—Logarithmic polar projections of the CO intensity and velocity maps. Although the origin of the abscissa (azimuthal angle) is arbitrary, in this case it is aligned with due north. The direction of rotation is to the right (counterclockwise as seen on the sky). Also shown are the two logarithmic spiral lines positioned along the two spiral arms, which correspond to the lines overlaid on the maps of Fig. 1.

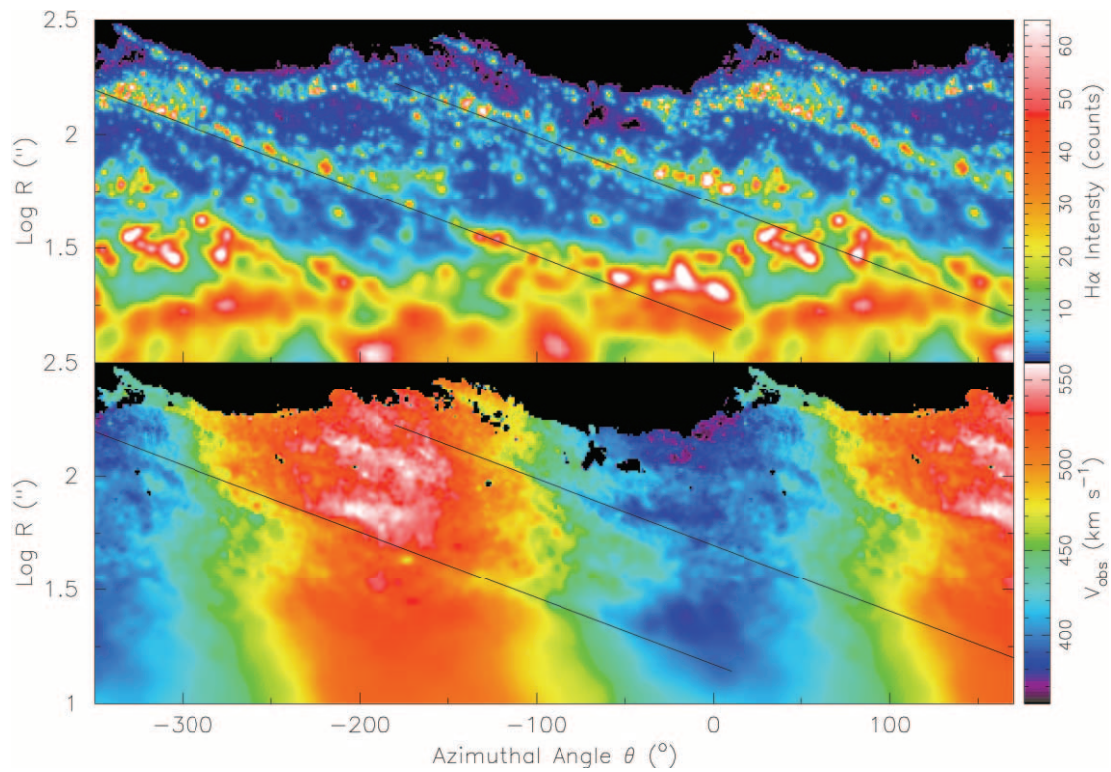


FIG. 5.—Logarithmic polar projections of the H $\alpha$  intensity and velocity maps. Coordinate system and log spiral overlays are as in Fig. 4.

TABLE 1  
INITIALLY ADOPTED PARAMETERS FOR M51

Parameter	Value	Reference
Center R.A. ( $\alpha$ ; J2000.0).....	13 <sup>h</sup> 29 <sup>m</sup> 52.71 <sup>s</sup>	Hagiwara et al. (2001)
Center decl. ( $\delta$ ; J2000.0).....	47°11'42.80"	Hagiwara et al. (2001)
Systematic velocity ( $V_{\text{sys}}$ ).....	472 km s <sup>-1</sup> (LSR)	Tully (1974)
Position angle of major axis ( $\theta_{\text{MA}}$ ).....	170°	Tully (1974)
Inclination ( $i$ ).....	20°	Tully (1974)

angle, and inclination are required. We initially use the canonical values for these parameters, which are listed in Table 1. We discuss the estimation of these parameters in the next section.

The two straight lines overlaid on Figures 4 and 5 indicate the adopted pitch angle of 21.1° and also correspond to the spiral loci shown in Figure 1. It is clear from the overlaid lines, which are separated by 180°, that the weaker arm is not symmetric with the brighter one, as discussed by Henry et al. (2003). Yet, both CO arms wrap around approximately 360° of the galaxy, even though they appear to jump in phase at one or more positions. The arms in H $\alpha$  show more jumps in phase and variations in the pitch angle. In spite of their asymmetries, the CO spiral arms are particularly well described as logarithmic spirals, better even than H $\alpha$  or the optical arms shown by Elmegreen et al. (1989).

We will refer to overlaid logarithmic spiral arcs (or lines) as “slits,” for we will extract observed CO and H $\alpha$  velocities as a function of position along the arc (or line), similar to obtaining long-slit spectra. Each slit marks a region of constant arm phase  $\psi$ . Thus, while the observed velocity varies along the slit due to projection,  $v_R$  and  $v_\theta$  are assumed constant. We arbitrarily define the arm phase marked by the leftmost slit in Figures 4 and 5 as  $\psi = 0^\circ$ . The other CO arm appears at an arm phase of approximately  $\psi = 180^\circ$ ; other features such as the stellar arms and the gravitational potential minimum may of course be offset from the CO arms.

As noted previously, our fit will assume that the intrinsic  $v_R$  and  $v_\theta$  are constant at a given arm phase, i.e., along a given slit, but that  $v_R$  and  $v_\theta$  vary with  $\psi$  as the slit is translated in azimuth. Translating the slit amounts to shifting a straight line to the right in the logarithmic polar diagram; this direction of increasing azimuth is the same as the direction of rotation for M51. We then fit equation (2) to the observed velocities extracted at each arm phase  $\psi$ , thereby obtaining  $v_R(\psi)$  and  $v_\theta(\psi)$ .

Although  $v_R$  and  $v_\theta$  vary primarily with arm phase, they may of course also vary with radius. Therefore, we limit the radial range of an annulus (or equivalently the length of a slit) as much as possible while still fitting a sufficiently extended azimuth range to obtain good leverage on both  $v_R$  and  $v_\theta$ . In other words, an annulus should be sufficiently broad to cover the spiral arm both near the major axis and the minor axis; the width of the annulus thus depends on the pitch angle and galactocentric radius of the arm.

We first test our method by applying it to a model spiral galaxy with known radial and tangential velocities. The solid lines in Figure 6 show the averaged density,  $v_R$ , and  $v_\theta$  profiles in an annulus from a snapshot of a hydrodynamic simulation of a disk responding to a spiral perturbation. The model spiral galaxy is a 2D version of a 3D model described in detail in Gómez & Cox (2002), and the annulus used here extends from 8.38 to 8.92 kpc. The direction of gas flow is in the direction of increasing phase. As the gas approaches the arm (marked by density maxima), the radial velocity  $v_R$  decreases by  $\sim 40$  km s<sup>-1</sup>. The sign reversal of  $v_R$  indicates that the gas is moving away from the nucleus before the shock and toward the nucleus after the shock. As the gas

emerges from the arm, the radial velocity increases again. The tangential velocity  $v_\theta$  gradually decreases as the gas approaches the arm, then receives a strong boost and reaches a maximum just downstream from the arm.

In order to test the fitting algorithm, the model  $v_R$  and  $v_\theta$  at all locations are used in equation (1) to create a model observed velocity field. This velocity field, along with the model density map, is transformed into logarithmic polar projections. Equation (2) is then fit to the model observed velocities at each arm phase in an annulus using slits parallel to the spiral arms; the dashed lines in Figure 6 are the results of the velocity fits, in the same annulus (8.38–8.92 kpc). The results reproduce the overall shape of the velocity profiles quite well, although with slight phase shifts and offsets. The offsets and the shallower minimum in  $v_R$  are likely due to the variation of the pitch angle of the arms with radius; i.e., the

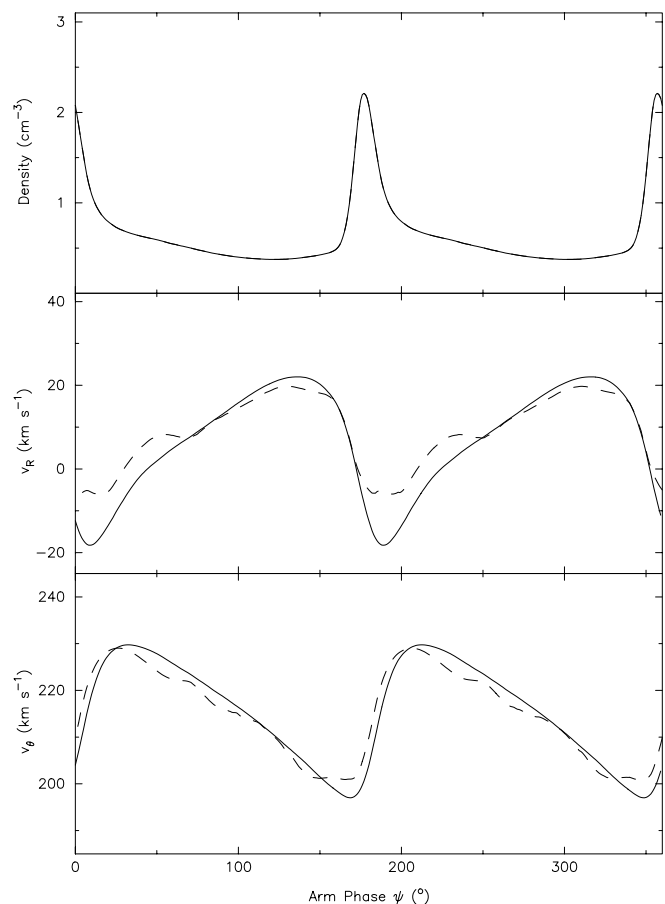


FIG. 6.—Gas profiles as a function of arm phase  $\psi$  for a model spiral galaxy (see text). Solid lines: Density (top),  $v_R$  (middle), and  $v_\theta$  (bottom) profiles averaged at each arm phase, in an annulus extending from 8.38 to 8.92 kpc. The  $v_R$  and  $v_\theta$  dashed lines in the two lower panels are obtained by fitting eq. (2) to the “observed” velocities in the 8.38–8.92 kpc annulus.

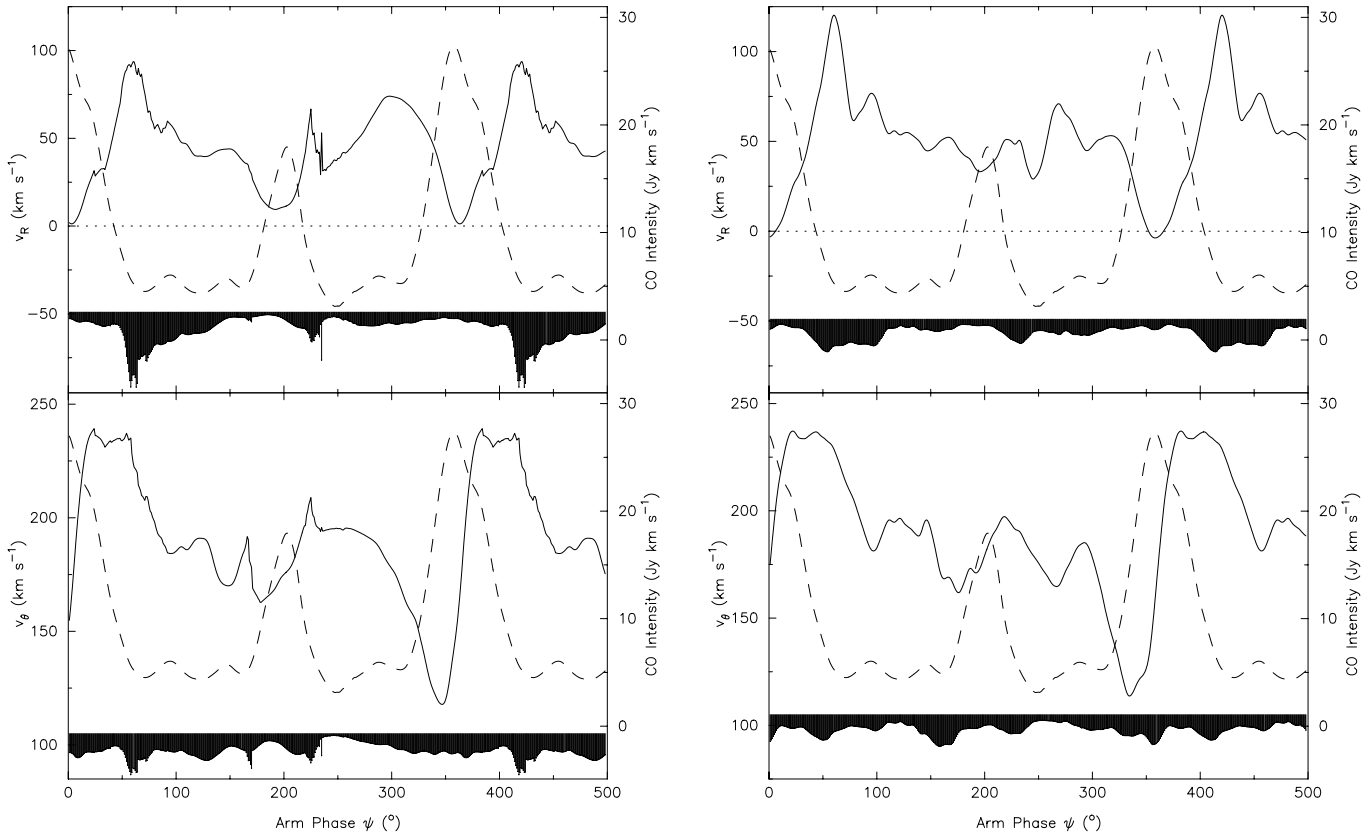


FIG. 7.—CO (left) and H $\alpha$  (right)  $v_R$  and  $v_\theta$  fits as a function of arm phase for an annulus with an inner radius of  $21''$  and an outer radius of  $36''$ . The one-sided  $3\sigma$  error bars are also shown on the bottom of each panel. Dashed lines are the corresponding mean CO velocity-integrated intensities, with the scale depicted on the right ordinate. Table 1 shows the fixed (canonical) parameters used in obtaining these fits.

spiral arms are not perfectly logarithmic, whereas the “slit” used to extract velocities at constant arm phase is. Despite these offsets, we were able to reproduce the major features of the velocity profiles of the model spiral galaxy, indicating that our method of fitting observed velocities at each arm phase recovers a 2D velocity field reasonably accurately.

We now apply our fitting method to the M51 data, adopting systematic parameters listed in Table 1. As an example, Figure 7 shows the  $v_R$  (top) and  $v_\theta$  (bottom) fits to the observed CO and H $\alpha$  velocity field for one annulus between the galactocentric radii of  $21''$  and  $36''$ . The CO intensity averaged along a slit as a function of phase angle  $\psi$  is also shown as dashed lines, indicating the distribution of molecular gas. As mentioned,  $\psi = 0^\circ$  is arbitrary and is marked by the leftmost line in Figures 4 and 5, corresponding to the brighter arm, which we will refer to as arm 1. We show a phase range greater than  $360^\circ$  so that both upstream and downstream velocities can easily be seen for both arms. The direction of gas flow through the arms (assuming we are inside corotation) is from left to right, so that the right sides of the CO peaks correspond to the downstream side of the arm. In most cases, as the gas flows through the arm, the radial velocity decreases and then increases, and the tangential velocity receives a boost, as predicted qualitatively by density wave theory.

In a conventional tilted-ring velocity fitting analysis, galaxy parameters such as the inclination, position angle, dynamical center, and systematic velocity can be directly fit. However, even though the inclination and position angle appear explicitly in equation (2), for our fits all but the systematic velocity must be assumed prior to deprojecting a galaxy velocity field and therefore before the fit. For our initial fits we employed the standard assumed values for these parameters for M51, shown in Table 1.

In the next section we explore the effects of errors in these assumed global parameters on the estimation of  $v_R$  and  $v_\theta$ .

#### 4. METHOD TESTING AND PARAMETER CONSTRAINTS

To test the sensitivity of the  $v_R$  and  $v_\theta$  fits to errors in the global (fixed) parameters, we generated test velocity fields and created sky projections with known parameters. We then applied our fitting technique to estimate  $v_R$  and  $v_\theta$  for the model galaxies, assuming incorrect values for the fixed parameters, and compared the fitting results to the actual model values of  $v_R$  and  $v_\theta$ . This enables us to quantify the sensitivity of the fits to the fixed parameters. In addition to constraints obtained from fitting our kinematic data, we also use standard methods to constrain the values of  $V_{\text{sys}}$ ,  $\theta_{\text{MA}}$ , and  $i$ . As we shall show, one of our conclusions is that some of the basic parameters for M51, many of which date to Tully (1974), may in fact be poorly constrained due to the morphological and kinematic perturbations induced by the tidal interaction with its companion.

As an initial test, we generated a simple model with  $v_\theta = 240 \text{ km s}^{-1}$  and  $v_R = -35$ , i.e., an axisymmetric disk with a flat rotation curve and uniform radial inflow. We refer to this model as the “constant velocity” model. We apply our general method to fit  $v_R$  and  $v_\theta$  as a function of arm phase using “observed” velocities. If we assume the input values of  $V_{\text{sys}} = 464 \text{ km s}^{-1}$ ,  $\theta_{\text{MA}} = 170^\circ$ , and  $i = 20^\circ$ , we indeed recover the input values for  $v_R$  and  $v_\theta$  as independent of phase. We now consider the effects of assuming incorrect values for the parameters.

##### 4.1. Position of Dynamical Center

In testing the sensitivity of the fits to the assumed center position, we applied the fitting algorithm to a model for which the

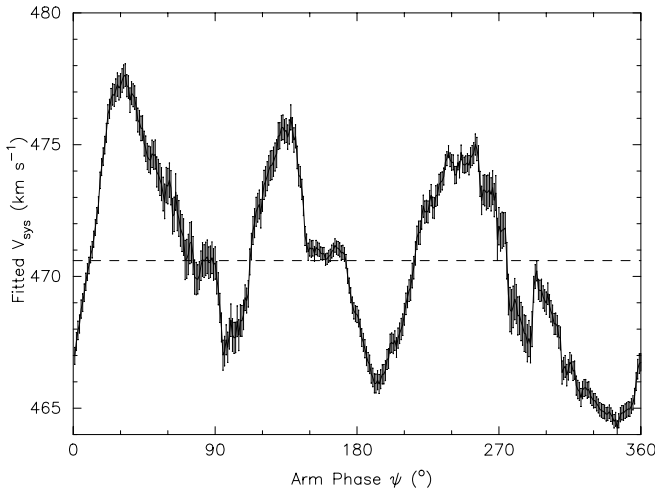


FIG. 8.—Result of fit to M51 CO velocity data in which  $V_{\text{sys}}$ ,  $v_R$ , and  $v_\theta$  were allowed to vary. The radial range of the annulus is  $14''$ – $136''$ . The fact that the fit value of  $V_{\text{sys}}$  varies with phase  $\psi$  shows that other parameters (e.g.,  $i$ ,  $\theta_{\text{MA}}$ ) vary with radius within the annulus. The mean of the fits is  $470.6 \text{ km s}^{-1}$  (LSR), shown by the dashed line.

center position was shifted by  $1''$  in both right ascension and declination. We found that a  $1''$  error in the assumed center has a negligible effect on the fit velocities. BIMA observations have an astrometric accuracy of  $\sim 10\%$  of the synthesized beam. The highest resolution of our CO observations is  $4.5''$ , so the error in position will likely not be greater than  $\sim 0.5''$ . Thus, observational errors will likely not affect the results of our fits. For all the analysis that follows, we will adopt the center position listed in Table 1. This choice assumes that the dynamical center coincides with the location of a weak AGN known to exist in the nucleus of M51 (Ho et al. 1987; Nakai & Kasuga 1988). We use the position of the radio continuum source observed with the VLA, which has an accuracy of  $\pm 0.01''$  (Hagiwara et al. 2001).

#### 4.2. Systematic Velocity

Before discussing methods for determining  $V_{\text{sys}}$ , we first explore the effect that an error in an assumed value of  $V_{\text{sys}}$  would have on fits for  $v_R$  and  $v_\theta$  in which  $V_{\text{sys}}$  is held fixed, using the constant-velocity model. As expected, an error  $\Delta V_{\text{sys}}$  in the assumed  $V_{\text{sys}}$  produces a sinusoidal variation in both fitted velocity components, with an amplitude of  $\Delta V_{\text{sys}}/\sin i$  and a period of  $360^\circ$  (see eq. [1]). Clearly,  $V_{\text{sys}}$  needs to be well determined.

One approach to obtaining  $V_{\text{sys}}$  is to fit the data for its value using equation (2). Figure 8 shows the results of fits to the M51 data in which  $V_{\text{sys}}$  was fit, along with  $v_R$  and  $v_\theta$ , as a function of arm phase. Although  $V_{\text{sys}}$  should be constant, it can be seen that the fit value of  $V_{\text{sys}}$  varies with arm phase. Similar variations in fitted  $V_{\text{sys}}$  result regardless of what values of the position angle and inclination are assumed.

One possible explanation for the apparent variation of  $V_{\text{sys}}$  is that the galactic disk of M51 is twisted and/or warped, i.e., the position angle and/or inclination may vary with radius. We therefore compare the results of fitting for  $V_{\text{sys}}$  from a model galaxy with no warp to a model with a warp. We again make use of the constant-velocity model, for this model also represents an unwarped disk. Instead of keeping  $V_{\text{sys}}$  fixed, we allowed this parameter to be free in the fit. If we use the true position angle and inclination, we correctly recover the adopted values for all three free parameters,  $V_{\text{sys}}$ ,  $v_R$ , and  $v_\theta$ .

To generate a warp model, we increase  $i$  monotonically from  $25^\circ$  at the inner radius ( $100''$ ) to  $35^\circ$  at the outer radius ( $200''$ );

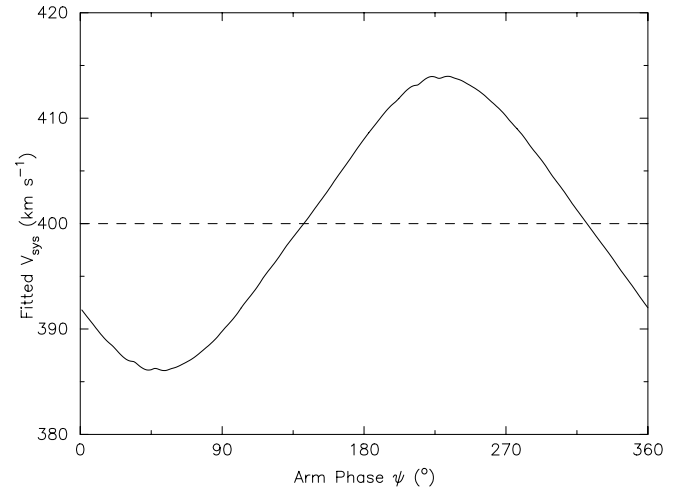


FIG. 9.—Fitted  $V_{\text{sys}}$  as a function of arm phase, similar to Fig. 8, but for a model galaxy with a warp. The systematic velocity adopted for the model is  $400 \text{ km s}^{-1}$  (dashed line), equal to the mean of the fits (solid line).

the position angle is kept fixed. If we allow  $V_{\text{sys}}$  to be free in fitting the model data, Figure 9 shows that the  $V_{\text{sys}}$  varies almost sinusoidally about the true model value  $400 \text{ km s}^{-1}$ . The mean fitted systematic velocity is equal to this value. This is the case regardless of what values of inclination or position angle we use (within reasonable limits), and regardless of the radius range of the annulus used for fitting. Thus, regardless of the assumed fixed parameters and of the limits in radius, for a simple warp the mean value of the fits gives the correct systematic velocity.

Motivated by our finding that even with a warp the average fit value of  $V_{\text{sys}}$  gives the true value, we calculated the mean of the  $V_{\text{sys}}$  values shown in Figure 8, obtaining  $V_{\text{sys}} = 470.6 \text{ km s}^{-1}$ . Comparison of the  $V_{\text{sys}}$  fits of the actual M51 data (Fig. 8) with  $V_{\text{sys}}$  fits to the simple warp model (Fig. 9) shows that the warp model has a slower variation. Hence, if a warp is responsible for producing variations in the fitted systematic velocity it must be more complex than our simple model; we return to this question in § 6.2.

We therefore apply two additional methods to estimate the value of  $V_{\text{sys}}$ . The first method is based on a standard tilted-ring analysis (Begeman 1989), in which the galactic disk is represented as a series of nested tilted rings. In its most general form, each tilted ring may have a different center, systematic velocity, position angle, inclination, and rotational velocity. We use  $10''$  rings from an inner radius of  $20''$  to an outer radius of  $120''$ , fixing the center position, inclination, and position angle to the values in Table 1. We obtain a mean systematic velocity of  $471.4 \pm 0.5 \text{ km s}^{-1}$ . When we allow the position angle to vary as well, we obtain a mean of  $471.3 \pm 0.3 \text{ km s}^{-1}$ .

A third method we use to constrain  $V_{\text{sys}}$  is to assume a functional form for the rotation curve, using the NEMO program `rotcurshape` (Teuben 1995). In contrast to the tilted-ring method, which fits each ring independently, `rotcurshape` fits  $V_{\text{sys}}$ ,  $\theta_{\text{MA}}$ ,  $i$ , center position  $\alpha$  and  $\delta$ , and the coefficients of the function used to describe the rotation curve simultaneously to the entire velocity field. Therefore, it can yield a single  $V_{\text{sys}}$  that best fits the entire velocity field. It is particularly useful for finding  $V_{\text{sys}}$  if the kinematic center position can be fixed. For this fit, we limit the `rotcurshape` fit to the inner  $20''$  in radius. This is inside the main spiral arms, in the region where the rotation curve is rising and the isovelocity contours are relatively straight. We assume the center,  $\theta_{\text{MA}}$ , and  $i$  listed in Table 1 and a rotation curve of

TABLE 2  
ESTIMATION OF THE SYSTEMATIC VELOCITY OF M51

Method	$V_{\text{sys}}^a$ (km s <sup>-1</sup> )	Error (km s <sup>-1</sup> )
Tully (1974).....	472	3
Freeing $V_{\text{sys}}$ in fitting for $v_R(\psi)$ and $v_\theta(\psi)$ .....	470.6	0.4
Tilted-rings analysis.....	471.4	0.5
Rotation-curve fitting.....	473.3	0.5
Weighted mean .....	471.7	0.3

<sup>a</sup> Velocity in LSR frame.

the form  $v = V_{\text{sys}} + v_0x/(1 + x)$ , where  $x$  is the ratio of the radius to the core radius, and fit for  $V_{\text{sys}}$ ,  $v_0$ , and the core radius. We obtain  $V_{\text{sys}} = 473 \pm 0.5$  km s<sup>-1</sup>. If we allow the position angle to vary as well, we obtain  $473.2 \pm 0.3$  km s<sup>-1</sup>. It is encouraging that this is within 2 km s<sup>-1</sup> of  $V_{\text{sys}}$  determined from the other two methods even though this fit uses a different method and fits an entirely different region (i.e., the inner 20'', inside the main CO arms, as opposed to outside 20'').

The canonical value of  $V_{\text{sys}}$  for M51 is  $472 \pm 3$  km s<sup>-1</sup> (Tully 1974 and references therein). Table 2 lists Tully's value for  $V_{\text{sys}}$  as well as the results from applying the three techniques described above. Our different methods give a mean systematic velocity of  $471.7 \pm 0.3$  km s<sup>-1</sup>. Henceforth, we will fix  $V_{\text{sys}}$  to be 472 km s<sup>-1</sup> (LSR, corresponding to a heliocentric velocity of 464 km s<sup>-1</sup>) in fitting the velocity field to estimate  $v_R(\psi)$  and  $v_\theta(\psi)$ .

### 4.3. Position Angle

To investigate the effect of errors in the assumed galaxy position angle on the fitted values of  $v_R$  and  $v_\theta$ , we first use the aforementioned constant-velocity model. Note that the position angle is required to deproject the galaxy image, as well as in equation (2). Using incorrect position angles, but correct model values of systematic velocity and inclination, yields a greater effect on  $v_R$  than on  $v_\theta$ . This is because an error  $\Delta\theta_{\text{MA}} \ll 1$  in  $\theta_{\text{MA}}$  results in an error  $\approx -v_\theta \sin \Delta\theta_{\text{MA}}$  in the fitted  $v_R$ , whereas the corresponding error in  $v_\theta$  is  $\approx +v_R \sin \Delta\theta_{\text{MA}}$ . Since  $v_\theta$  is large compared to  $v_R$ , the shift in  $v_R$  is larger than the shift in  $v_\theta$ . Thus, a  $\pm 10^\circ$  error in position angle in the constant-velocity model that has  $v_\theta = 240$  km s<sup>-1</sup> produces approximately a  $\mp 40$  km s<sup>-1</sup> shift in the fitted radial velocity. Position angle errors also produce small perturbations in both velocity components. We conclude that using an accurate value of  $\theta_{\text{MA}}$  is very important to obtain accurate  $v_\theta$  and especially  $v_R$  fits.

Unfortunately, the position angle of the major axis of M51 is particularly difficult to determine. The strong spiral arms and the tidal interaction with NGC 5195 distort the stellar disk, making it effectively impossible to determine a position angle from the orientation of the isophotes. Thus, it is necessary to go beyond morphology in determining  $\theta_{\text{MA}}$ . We therefore revisit the determination of the galaxy's position angle. We apply the method of Tully (1974) to our velocity data from H $\alpha$  and CO observations. We also study the effect of streaming motions on this method by using model galaxies with known position angles and streaming velocities. In addition, we also apply two alternate methods to derive the position angle.

The widely used value for the position angle of M51,  $170^\circ$ , was determined by Tully (1974) using kinematic information. Tully assumed that the observed velocity should reach its extreme value at the position angle of the galaxy major axis,  $\theta_{\text{MA}}$ . To determine  $\theta_{\text{MA}}$ , he averaged the observed velocities in wedges

extending over  $5^\circ$  in azimuth, and then for each radius took the position angle of the wedge with the extreme velocity as the estimated major axis at that radius. Tully excluded radii at which he was not confident that the true major axis had measured velocities (e.g., the faint interarm regions near the major axis).

Figure 10 shows the results of applying Tully's position angle determination method to H $\alpha$  and CO observations. For each annulus of radial extent  $5''$ , the position of the wedge with the extreme velocity is marked. Due to the lack of data in the outer regions of the CO observations, only the wedges in the inner  $70''$  provide reliable measures of the position angle of the extreme velocity. Similar to Tully, we did not attempt to estimate the position angle of the extreme velocity at radii for which data are sparse in the range of plausible position angles of the major axis. From the location of these extreme velocity wedges, we found  $\theta_{\text{MA}}$  to be  $172^\circ$  (from an error-weighted average) from both CO and H $\alpha$  observations.

However, streaming motions can shift the velocities, resulting in the extreme velocity occurring at position angles not corresponding to the true major axis. Indeed, inspection of positions of the velocity extremum wedges overlaid on the intensity maps shows that the position angles of the wedges in the interarms are clearly shifted counterclockwise from those in the arms. This is most evident in the H $\alpha$  maps, for which emission is detected from almost everywhere in the disk. We further explore streaming effects on the Tully method using a model with known streaming motions, generated using one of our  $v_R$  and  $v_\theta$  fits to the M51 CO data, with  $\theta_{\text{MA}} = 170^\circ$ . (Since this test is designed simply to reveal the twists in the apparent position angle due to streaming, the particular value assumed for the true position angle and the particular  $v_R$  and  $v_\theta$  fits used is not significant.) Figure 11 shows the results of applying Tully's method to this streaming model galaxy. In any given annulus, the extreme velocity averaged in the  $5^\circ$  wedges occurs in the interarm regions. In Tully's analysis, however, only spiral-arm regions (near the apparent major axis) were considered, due to observational limitations. Therefore, the major axis position angle he found is likely biased clockwise from the true major axis. As shown in Figure 11, even if the interarm regions are considered, the position angles of the locations of the extreme velocities do not necessarily correspond to the major axis. Thus, such an extrema method can be biased due to the inherent streaming in M51, regardless of whether the arms or interarms are considered.

We employ two alternate position angle determination methods that make use of the full observed velocity field. In the first method, we average the observed velocity at each position angle in a wedge for both the northern and southern sides of the galaxy; then we fit a cosine curve to these averaged velocities as a function of azimuthal angle. We will refer to this method as the "radial-averaged" method. This is most easily accomplished in the polar projection, where we can average along a column to perform the radial average. The radial-averaged velocity as a function of position angle is shown in Figure 12, along with the corresponding cosine fitted curves. We assume that the galaxy major axis should be at the position angle of the extrema of such curves. The mean position angle determined from the H $\alpha$  and CO fits is  $\sim 177^\circ$ , larger than the position angle determined by the Tully method. Again, the position angle determined in such a way is sensitive to streaming. Earlier we showed that streaming tends to cause the position angle of extreme interarm velocities to be biased counterclockwise from the true value. Since the interarms occupy a greater fraction of the galaxy compared to the arms, streaming will introduce a counterclockwise bias to the apparent position angle of the major axis. The effect of streaming on this

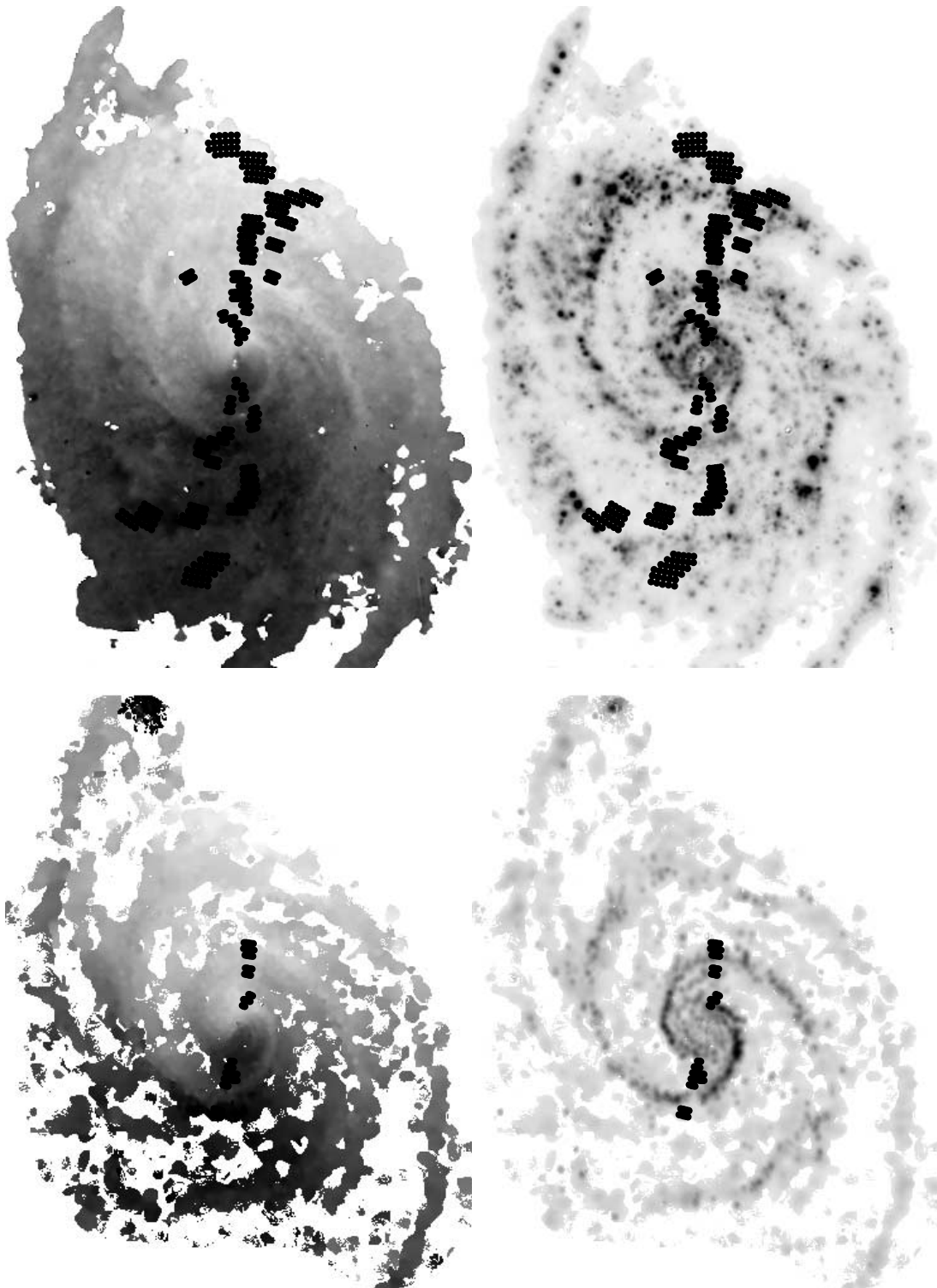


FIG. 10.—Tully “wedge” method for estimating galaxy position angle. The extreme velocity for each  $5''$  annulus, averaged in  $5^\circ$  wedges, is marked. The top panels show the H $\alpha$  velocity (*left*) and velocity-integrated intensity (*right*); bottom panels show the same for CO. For CO, emission was too weak to apply the method at some radii, especially in the outer galaxy.

method is further discussed below, following a discussion of our second position angle determination method.

Our second method to determine the position angle, the “azimuthal fit” method, is similar to the one described in the previous paragraph, but instead the cosine curve is fit to the ob-

served velocities along a projected circle with constant (projected) radius. As in the previous method, the polar projection of the velocity field is useful; in this case we simply fit a cosine curve to the velocities along a row of constant projected radius. The results from applying this method are shown in Figure 13. Note

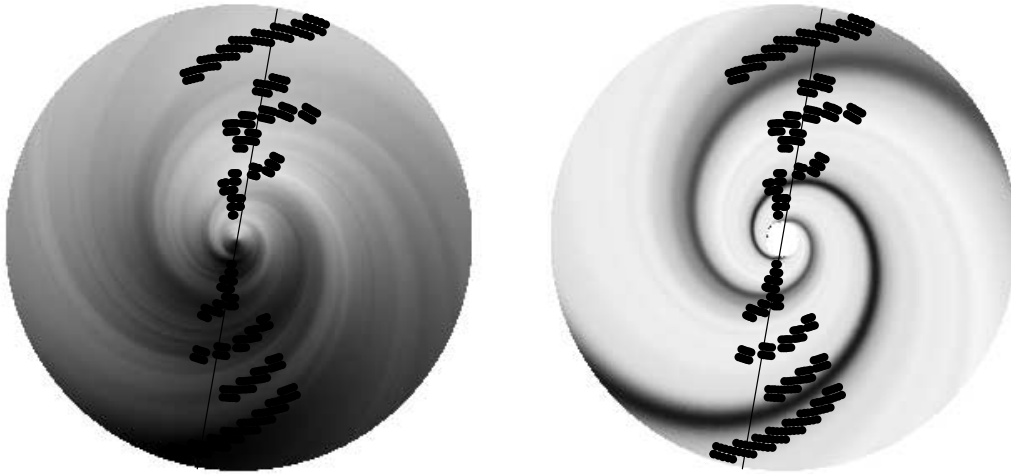


FIG. 11.—Application of Tully wedge method to a model with streaming. The velocity field is shown (*left*) along with the corresponding intensity map (*right*). The position angle assumed in the model is  $170^\circ$ , shown by the solid line. The  $5^\circ$  wedges with the extreme velocity for each annulus is marked. It can be seen that streaming shifts the estimated position angle from the true position angle. Note that the extreme velocities do not occur in the arm.

that the position angle of the velocity extrema varies systematically as a function of radius; it is approximately  $180^\circ$  in the inner region  $30''$  from the center, declining to  $165^\circ 120''$  from the center; this trend, including the rise near  $\log R = 1.7$ , is also evident from simple inspection of Figures 4 and 5. Averaging over the radius range displayed in Figure 13, we obtain the same position angle of  $\sim 177^\circ$  as in the previous method. Again, the velocities

in the interarms bias this determination of position angle, for the same reasons stated in the previous paragraph.

In order to understand the effect of streaming motions on the position angle of the major axis derived using the radial-averaged and azimuthally fit methods, we apply these methods to streaming models with known position angles and streaming velocities. The model velocity fields are produced from our  $v_R$  and  $v_\theta$  profiles

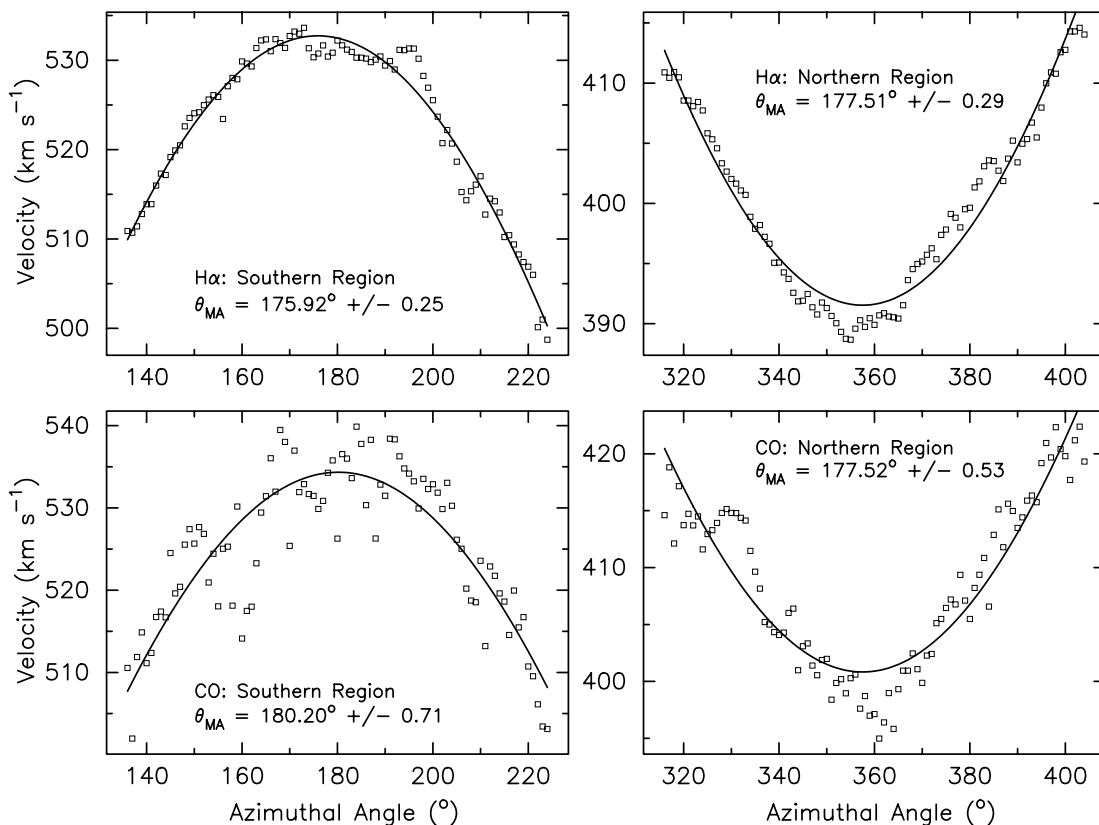


FIG. 12.—Mean observed velocity plotted vs. azimuthal angle. All observed velocities were averaged over radius at each azimuth. Velocities are fit by cosine functions (*solid line*); extremum of the cosine curve indicates the best-fit position angle of the major axis.

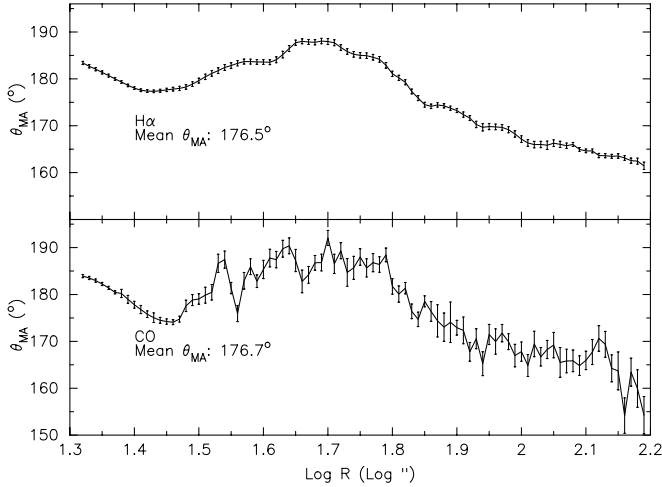


FIG. 13.—Fit position angle of the major axis  $\theta_{MA}$  as a function of galactocentric radius from H $\alpha$  (top) and CO (bottom) velocity fields. The position angles were obtained by fitting a cosine function to the distribution of observed velocity vs. azimuthal angle at each radius.

obtained by assuming fixed values of  $\theta_{MA}$ ; we then apply the radial-averaged and azimuthally fit methods to these model velocity fields. Both methods recover a  $\theta_{MA}$  of  $\sim 176^\circ$  for all models, similar to the actual M51 velocity field, even though the position angles assumed in generating the streaming models can be very different. This is because for different position angles, the streaming velocities were derived from fits designed to best match the observed velocities. So in fact all the streaming models give virtually identical observed velocity fields regardless of assumed position angle.

However, if we recreate the models setting the radial component to be zero everywhere, then we correctly recover the assumed position angles. This is clear evidence that radial streaming affects methods to determine  $\theta_{MA}$ , not only near the minor axis, as recognized by Tully, but also elsewhere, including even the major axis.

In order to quantify the effect of the nonzero radial velocities on the apparent position angle, we apply the position angle determination methods to models with known constant radial velocities. In these artificial models tangential streaming velocities are assumed to vary with arm phase, but radial streaming is assumed constant. We found that for every  $\pm 10 \text{ km s}^{-1}$  in radial velocity, the derived position angle differs from the actual position angle by  $\pm 3^\circ$ . This degeneracy between the position angle and radial velocity renders it difficult to accurately identify the true position angle, or to map the radial velocity. In order to accurately determine the position angle, we need to know the radial streaming. But in our effort to map the radial and tangential velocities of M51, we need to know the position angle. Thus, as we carry out our investigation, we shall use a range of position angles in deriving the two-dimensional velocity components of M51.

#### 4.4. Inclination

Estimating the inclination based on the orientation of the isophotes is unreliable, as discussed in § 4.3, due to the strong perturbations from the spiral arms and the tidal interaction. In principle, the inclination can be determined from a fit to the velocity field, as we did to obtain the systematic velocity in § 4.2. However, the fit inclination is not well determined by the available data, presumably due to the streaming. To test the sensitivity of the  $v_R$  and  $v_\theta$  fits to the inclination  $i$  in equation (2), we assume incorrect values of the inclination that differ from the true value by

$\Delta i$  for the constant-velocity model (where  $v_R$  and  $v_\theta$  are constant). We then fit for  $v_R$  and  $v_\theta$ . As expected, an error  $\Delta i$  results in errors in the fit value of  $v_R$  and  $v_\theta$  with magnitudes  $\propto \sin \Delta i$ , along with small perturbations about this offset.

Since we find that errors introduced in the velocity components due to an incorrect inclination can be large (although just a simple scaling), we sought other constraints on the inclination. In particular, the Tully-Fisher (Tully & Fisher 1977) relation can be used to estimate the inclination. The well-known Tully-Fisher relation is a correlation between galaxy luminosity and maximum rotation speed. The inclination can be estimated by comparing the rotational velocity predicted by the Tully-Fisher relation with the observed velocity of the flat part of the rotation curve. We use the baryonic form of the Tully-Fisher relation discussed by McGaugh (2005; see also McGaugh et al. 2000):

$$M_b = 50V_c^4, \quad (3)$$

where  $M_b$  is the baryonic mass (in  $M_\odot$ ) and  $V_c$  is the circular rotational velocity (in  $\text{km s}^{-1}$ ). Since the dispersion in the Tully-Fisher relation,  $L \propto V_c^4$ , is relatively small, given the luminosity the uncertainty in  $V_c$  is small.

In order to determine the baryonic mass  $M_b$ , we require the stellar mass  $M_*$ , which is related to the  $B$ -band luminosity  $L_B$  and the  $B$ -band mass to light ratio ( $M/L_B$ ),

$$M_* = L_B(M/L_B). \quad (4)$$

We use the correlation of the galaxy color with  $M/L$  discussed by Bell & de Jong (2001) applicable to the Charlot & Bruzual (1991) population synthesis models to obtain ( $M/L_B$ ):

$$(M/L_B) = 10^{[-0.63 + 1.54(B-V)]}. \quad (5)$$

The RC3 catalog (de Vaucouleurs et al. 1991) gives  $(B - V) = 0.53$  for M51, so  $(M/L_B) = 1.54$ .

The last quantity required to determine  $M_*$  is the luminosity  $L_B$ , which can be derived if we know the distance. Two independent studies have given similar M51 distance estimates: observation of planetary nebulae gives a distance modulus of  $m - M = 29.62 \pm 0.15$  (Feldmeier et al. 1997), and a study of surface brightness fluctuations in the companion NGC 5195 gives  $m - M = 29.59 \pm 0.15$  (Jensen et al. 1996). We thus employ a distance modulus of  $m - M = 29.6$ , corresponding to a distance of  $8.4 \pm 0.6 \text{ Mpc}$ . Using the RC3 catalog value of  $B = 8.67$ , corrected for extinction,

$$L_B = 10^{-0.4(8.67 - 29.6 - 5.48)} L_\odot = 3.66 \times 10^{10} L_\odot. \quad (6)$$

Using this value and the ( $M/L_B$ ) value of 1.54 (eq. [5]) in equation (4), we obtain

$$M_* = 5.64 \times 10^{10} M_\odot. \quad (7)$$

We can now apply the McGaugh (2005) relation in equation (3) to obtain the circular velocity:

$$V_c = [(M_* + M_{\text{gas}})/50]^{1/4} = 188 \text{ km s}^{-1}, \quad (8)$$

where  $M_{\text{gas}}$  is the total gas mass; in the case of M51 the gas is predominantly molecular. From our CO observations, we compute  $M_{\text{gas}} = 5.4 \times 10^9 M_\odot$ , using an X-factor of  $2 \times 10^{20} \text{ cm}^{-2} (\text{K km s}^{-1})^{-1}$  (e.g., Strong et al. 1988). Due to the small value of

the exponent in equation (8), errors in the mass, due to variations in the X-factor, for example, will not significantly affect the resulting rotational velocity.

The observed velocity is related to the circular velocity by

$$V_{c,\text{obs}} = V_c \sin i. \quad (9)$$

Adopting the center,  $\theta_{\text{MA}}$ , and  $V_{\text{sys}}$  described in this section, we apply a tilted-ring analysis to determine the flat part of the rotation curve. We obtain an observed circular velocity between 70 and 80 km s<sup>-1</sup>, implying

$$22^\circ \lesssim i \lesssim 25^\circ. \quad (10)$$

Therefore, for our subsequent fits, we adopt an inclination of 24°.<sup>1</sup>

#### 4.5. Summary: System Parameter Values

In summary, we have shown that the fit values of  $v_R$  and  $v_\theta$  are sensitive to the assumed values for the fixed parameters in equation (2),  $V_{\text{sys}}$ ,  $\theta_{\text{MA}}$ , and  $i$ . Uncertainties in the assumed position of the dynamical center are too small to significantly affect the derived streaming velocities. We have used three different methods to determine  $V_{\text{sys}}$ , which resulted in a value similar to the  $V_{\text{sys}}$  found by Tully. We have found it to be extremely difficult to constrain the value of the position angle of the major axis using the velocity field, due to the significant streaming that shifts the position angle of the extreme velocities. As a result, in fitting for  $v_R$  and  $v_\theta$ , we allow for a range of plausible position angles. Lastly, we adopt an inclination of 24°, which is determined by using the baryonic Tully-Fisher relation (McGaugh et al. 2000) between the baryonic mass and rotational velocity. To estimate  $v_\theta$  and  $v_R$ , we thus use the center position and systematic velocity listed in Table 1, but use a range of position angles and an inclination of 24°.

## 5. RESULTS: VELOCITY PROFILE FITS

With our improved estimates of the global parameters, we apply the fitting algorithm to the observed velocity field in different annuli to determine the radial and tangential velocities  $v_R$  and  $v_\theta$  as a function of arm phase  $\psi$ . We initially adopt a position angle  $\theta_{\text{MA}}$  of 170°. We address the issue of a varying  $\theta_{\text{MA}}$  in § 6.2. Figures 14 and 15 show the CO and H $\alpha$   $v_R$  and  $v_\theta$  fits in six overlapping annuli between galactocentric radii of 21'' and 105'', and Figure 16 shows the corresponding overlapping annular regions.

An initial inspection of the streaming profiles indicates that the velocity structure is rather complex. Models of density wave streaming qualitatively predict that as gas encounters the arm,  $v_R$ , which was positive (i.e., outward) in the interarm, becomes negative, and that as the gas exits the arm it again becomes positive. The azimuthal velocity  $v_\theta$  is predicted to increase rapidly as gas flows through the arm, and then decline more gradually in the interarm (e.g., Roberts & Stewart 1987 and § 3). First we concentrate on arm 1 (the brighter arm, shown at  $\psi = 0^\circ$  and more fully at 360°). For  $v_R$  there is a pronounced minimum close to the arm position, seen in both CO and H $\alpha$ . There is a boost in  $v_\theta$  through the arm, again seen in both CO and H $\alpha$ . For this arm, the streaming is qualitatively as expected from steady-state spiral-shock models. The velocities associated with arm 2 (located at  $\psi \sim 200^\circ$ ), however, do not agree with simple predictions. For

$v_R$ , a clear minimum is only apparent in the outer annuli, and the boost in  $v_\theta$  is weak or nonexistent. In the interarms, the structure appears somewhat more complex than the simple model expectation of a relatively constant or slowly rising  $v_R$  and a slowly declining  $v_\theta$ . We suggest that arm 1 matches simple theory because its structure is simple, i.e., well described as a log spiral of constant phase. By contrast, for arm 2 the CO distribution is not as well described by a single log spiral segment. Instead, it has several segments with different pitch angles and jumps in phase; thus the velocities associated with this arm are complex.

One explanation for the differences in the two arms, as discussed by Rix & Rieke (1993), is that the spiral pattern in M51 is actually a superposition of a strong spiral mode with a  $m = 2$  Fourier component with weaker  $m = 1$  and  $m = 3$  components. Henry et al. (2003), using the spatial distribution of CO emission obtained from the BIMA CO map, found such a scenario to be feasible by explaining the bright arm as the result of constructive interference between the  $m = 2$  and  $m = 3$  components, and the weak arm the result of a destructive interference between the two components. There is evidence for interarm structure possibly supporting such a multiple density wave component description of the spiral arms, which would be expected to manifest itself in the kinematics. Recent *Spitzer* observations of M51 clearly show spiral structure between the main CO arms; the *Spitzer* image and interarm features are discussed in the next section.

There are also clear differences between different annuli. For example, in the 36''–61'' annuli, the  $v_R$  increase downstream from the weaker arm is much more pronounced than in the 21''–36'' annuli. In addition, there is a  $v_R$  decrease to as low as  $< -50$  km s<sup>-1</sup> in the arms of the outer regions, which perhaps can be attributed to an incorrect choice of a fixed position angle for the disk (see § 4.3). There are also clear differences in the  $v_\theta$  gradients between different annuli.

By and large, similar velocity structure is apparent in both CO and H $\alpha$ . For example, in the 47''–80'' annulus, the gradual rise in  $v_R$  from  $-50$  km s<sup>-1</sup> at  $\psi = 180^\circ$  to 70 km s<sup>-1</sup> at  $\psi = 300^\circ$  is shown in both tracers. Further, there is a strong  $v_R$  peak at  $\psi = 120^\circ$  in the 27''–47'' annulus in both CO and H $\alpha$ ; however, such pronounced local extrema in the interarms are not expected in the theory for a single spiral mode. In general, the overall amplitude of the streaming and the location of most features coincide, and regions in which the velocity structure is somewhat different tend to be interarm regions where little CO is detected.

Such similarities are not unexpected due to the dynamical coupling between the different components. CO, which traces the molecular component, is dynamically cold, with a velocity dispersion of only 4–8 km s<sup>-1</sup>. Thus, the molecular component of the disk reacts strongly to any perturbation, as evident in the strong  $v_R$  and  $v_\theta$  gradients associated with the spiral arms. The spiral arms compress the gas, triggering star formation. The newly formed hot O and B stars subsequently ionize the surrounding gas, resulting in H $\alpha$  emission. Due to the fact that much of the H $\alpha$  emission comes from gas *near* the region of birth, observed H $\alpha$  velocities will be similar to observed CO velocities. There may also be a diffuse ionized medium not closely associated with the O and B stars, and this medium is likely not dynamically coupled with the molecular gas. However, as can be seen in Figures 4 and 5, the brightest regions of H $\alpha$  emission occur just downstream from the molecular spiral arms. Further, the generally good agreement between the velocity measurements from CO and H $\alpha$  observations suggests that most of the ionized emission originates in gas associated with star-forming regions. This similarity in velocity structure derived from independent observations also gives

<sup>1</sup> Employing the standard Tully-Fisher relation instead, we obtain a mean inclination of  $\sim 23^\circ$ , using the slope and zero-point fits from Verheijen (2001).

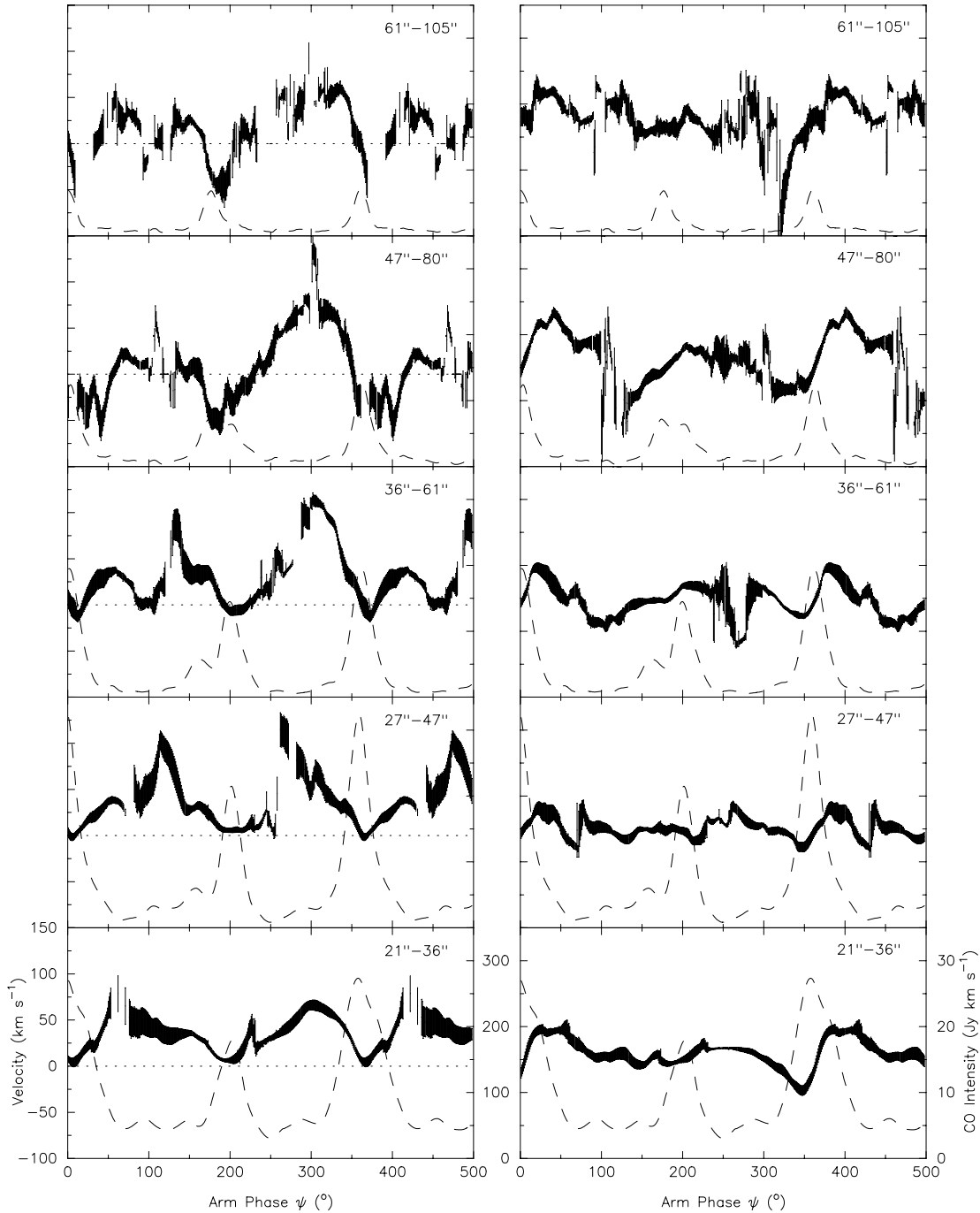


FIG. 14.—CO  $v_R$  (left panels) and  $v_\theta$  (right panels) fits as a function of arm phase  $\psi$  in different annuli (with radii labeled in the upper right of each panel). The thickness of the line shows a range of  $\pm 3\sigma$ . Only  $v_R$  and  $v_\theta$  fits with  $3\sigma \leq 20 \text{ km s}^{-1}$  and  $\leq 60 \text{ km s}^{-1}$ , respectively, are shown. Dashed lines are the corresponding mean CO intensities, with the scale shown on the right ordinate. We assume a position angle of  $170^\circ$ , an inclination of  $24^\circ$ , and the center position and systematic velocity listed in Table 1. Fig. 16 shows the annular regions of M51 considered for these fits.

confidence that the fitted velocities are reliable and that the deviations from simple theory, including interarm features, are real.

The profiles in Figures 14 and 15 qualitatively agree with previous studies of streaming in M51 involving 1D cuts along the major and minor axes (e.g., Rand 1993; Aalto et al. 1999). The gradients of the velocity profiles through the arms in different annuli is in accordance with the conclusion of Aalto et al. (1999) supporting the presence of shocks in the arms from a qualitative comparison of velocities along 1D cuts to streaming models of Roberts & Stewart (1987). In § 6 we analyze the fea-

sibility of a steady or quasi-steady spiral pattern in M51, which has been a working hypothesis for many analyses of the spiral arms of this galaxy.

### 5.1. Interarm Structure

In estimating the radial and tangential velocity components, we fit observed velocities along log-spiral segments. The slope of the slit is determined by the slope of the main CO arms on the logarithmic polar projection, i.e., the pitch angle of the arms. Although the slope of the CO arms, or at least the bright arm, is

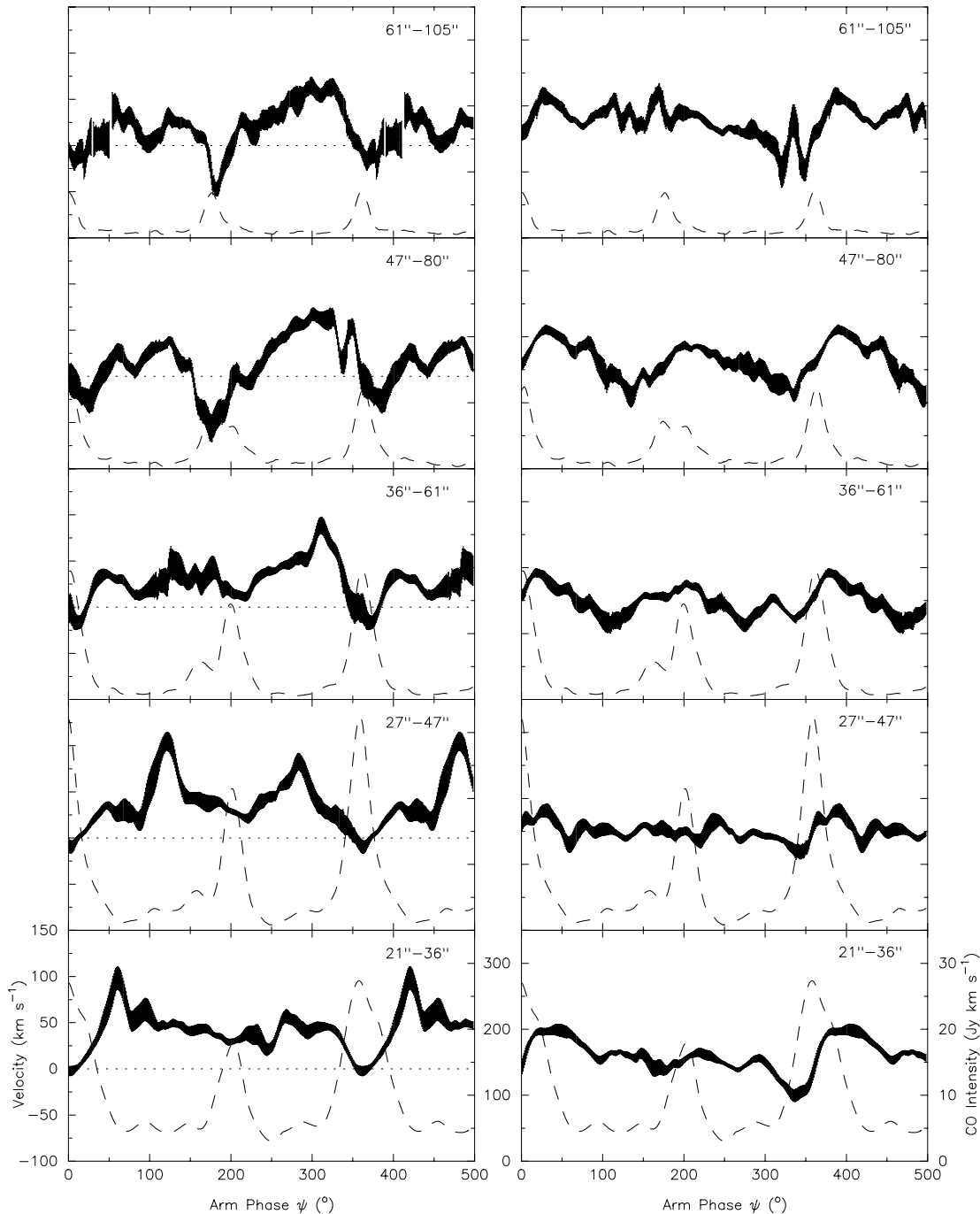


FIG. 15.— $H\alpha$   $v_R$  and  $v_\theta$  fits as a function of  $\psi$  in different annuli, as in Fig. 14.

well defined, that slope may not be appropriate for the interarms. In other words, velocity may not be constant along the interarm log-spiral segments congruent to the main CO arms.

The recent *Spitzer* 8  $\mu\text{m}$  image of M51 (Calzetti et al. 2005; Kennicutt et al. 2003) shows clear interarm features not seen in the CO map due to the lower resolution of the CO observations. Many of these features are spurs (or feathers) that have been found to be ubiquitous in grand-design spirals (La Vigne et al. 2006). These interarm features will also cause kinematic perturbations. In fact, close inspection reveals that interarm perturbations in the velocity field of M51 coincide with strong interarm features apparent in the 8  $\mu\text{m}$  image. Since the features have different pitch angles from the main CO arms, we are likely smearing out these finer interarm velocity perturbations. As a result, the inter-

arm velocity profiles we have derived do not reveal the details of the velocity perturbations associated with interarm substructure; in a detailed study of the 2D velocity field between the main arms, the interarm structure would need to be considered.

In the next section, we use the  $v_R$  and  $v_\theta$  fits to assess the feasibility of the hypothesis of a quasi-steady pattern. Again, our fitting method is designed to reveal streaming solely associated with the spiral arms, and does not capture smaller scale perturbations, such as those associated with interarm features. Both observations (Elmegreen 1980; La Vigne et al. 2006) and numerical simulations (Kim & Ostriker 2002; Shetty & Ostriker 2006) have shown that spurs and feathers are associated with star formation, indicating that these features are not long lasting. The modal theory, hypothesizing quasi-stationary grand-design

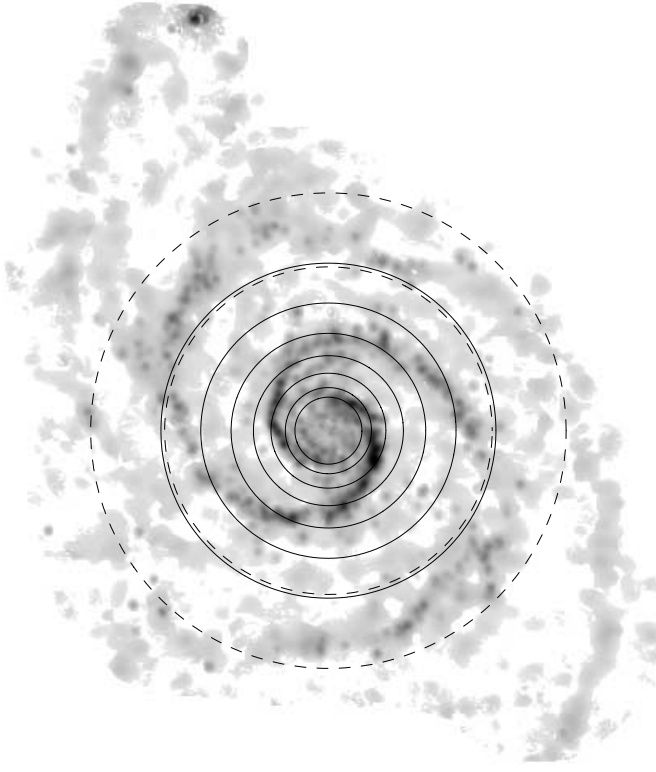


FIG. 16.—Deprojected CO map of M51 showing the overlapping annuli for which  $v_R$  and  $v_\theta$  are fitted as a function of arm phase (shown in Figs. 14 and 15). The radii of the solid circles, from the inner to the outer, are  $21''$ ,  $27''$ ,  $36''$ ,  $47''$ ,  $61''$ ,  $80''$ , and  $105''$ . The annulus marked by dashed circles ( $4.2 \text{ kpc} \leq R \leq 6.1 \text{ kpc}$ ) spans possible corotation radii corresponding to an adopted spiral pattern speed  $\Omega_p = 38 \pm 7 \text{ km s}^{-1} \text{ kpc}^{-1}$  (see § 6.2.2).

spiral structure, acknowledges that such smaller scale features can be transient (e.g., Bertin & Lin 1996). In this study, smearing out the interarm perturbations likely does not affect the overall conclusions we draw from the fitted velocity profiles.

## 6. TESTS OF CONSERVATION LAWS

### 6.1. Conservation of Vortensity

For a flattened system, the conservation of mass and angular momentum can be combined to yield

$$\frac{\partial}{\partial t} \left( \frac{\nabla \times \mathbf{v}_{\text{inertial}}}{\Sigma} \right) + \mathbf{v}_{\text{inertial}} \cdot \nabla \left( \frac{\nabla \times \mathbf{v}_{\text{inertial}}}{\Sigma} \right) = 0, \quad (11)$$

where  $\Sigma$  is the surface density and  $\mathbf{v}_{\text{inertial}}$  is the velocity in the inertial frame. Equation (11) states that the vorticity per unit surface density, known as vortensity, is conserved along stream-

lines. For steady systems, the conservation of vortensity can be simplified,

$$\frac{1}{\Sigma} \left( \frac{v_\theta}{R} + \frac{\partial v_\theta}{\partial R} - \frac{1}{R} \frac{\partial v_R}{\partial \theta} \right) = \text{constant}, \quad (12)$$

because the temporal term in equation (11) vanishes. Even if the flow is not steady, portions of the galaxy that originated in a region of constant vortensity will still satisfy equation (12).

In order to test whether equation (12) is satisfied for the gas in M51, we need the surface density  $\Sigma$ , which we can estimate using the observed CO brightness to derive the corresponding  $\text{H}_2$  column density.<sup>2</sup> Most studies suggest that the relationship between CO and  $\text{H}_2$  is reasonably linear, although the conversion factor, known as the X-factor, is controversial. In our analysis, we will assume that CO is indeed a linear molecular tracer, and employ an X-factor of  $2 \times 10^{20} \text{ cm}^{-2} (\text{K km s}^{-1})^{-1}$  (e.g., Strong et al. 1988).

We first test the vortensity condition from the velocity profiles derived in the  $47''$ – $80''$  annulus, (see Figs. 14–16). We choose this particular annulus because  $v_\theta$  variations are relatively smooth in both arm and interarm regions, and are likely due primarily to spiral streaming. This annulus clearly shows the characteristic  $v_\theta$  boost in the arm, and the more gradual interarm decrease in  $v_\theta$ . We consider the fits derived from this annulus assuming a  $\theta_{\text{MA}} = 170^\circ$  (see Fig. 13). As shown in § 4.3, changes in  $\theta_{\text{MA}}$  affect  $v_\theta$  only modestly.

For the first term in equation (12),  $v_\theta/R$ , we use the mean value of the tangential velocities fit in the given region. To measure the radial gradient of the tangential velocity, which appears in the second term, we use

$$\frac{\partial}{\partial R} \Big|_\theta = \frac{1}{R \tan i_p} \frac{d}{d\psi}, \quad (13)$$

where  $i_p$  is the pitch angle of the spiral arms, and we assume negligible variation parallel to the arm. We adopt a pitch angle of  $21.1^\circ$  (which is also the slope of the “slit”). We fit straight lines to the velocity profiles in order to approximate the last two terms in equation (12). For the surface densities, we use the peak value for the arm, and for the interarm we use the value of  $\Sigma$  at phase separated by  $90^\circ$  from the arm. Again, we are assuming that CO directly traces the molecular abundance. Table 3 shows the vortensity values for the  $47''$ – $80''$  annulus, including the values of each of the terms in equation (12).

Table 3 shows that, within the errors, the arms and interarm 2 have consistent vortensity values. The value for interarm 1,

<sup>2</sup> As we describe in § 6.2.2,  $\text{H I}$  can be neglected since the gas in M51 is mostly molecular in the region studied.

TABLE 3  
VORTENSITY IN THE  $47''$ – $80''$  ANNULUS

Region	$\Sigma^a$	$\left(\frac{v_\theta}{R}\right)^b$	$\left(\frac{\partial v_\theta}{\partial R}\right)^b$	$\left(\frac{1}{R} \frac{\partial v_R}{\partial \theta}\right)^b$	Vortensity Value <sup>c</sup>
Arm 1 ( $\psi \approx 360^\circ$ ).....	244	$70 \pm 1$	$103 \pm 2$	$-30 \pm 3$	$0.8 \pm 0.2$
Interarm 1 ( $\psi \approx 90^\circ$ ).....	16	$67 \pm 1$	$-52 \pm 3$	$6 \pm 1$	$0.5 \pm 0.2$
Arm 2 ( $\psi \approx 190^\circ$ ).....	128	$63 \pm 0.5$	$59 \pm 3$	$-18 \pm 3$	$1 \pm 0.2$
Interarm 2 ( $\psi \approx 275^\circ$ ).....	19	$59 \pm 1$	$-31 \pm 2$	$11 \pm 1$	$0.9 \pm 0.2$

<sup>a</sup> In units of  $M_\odot \text{ pc}^{-2}$ ; error of  $\sim 20\%$ .

<sup>b</sup> In units of  $\text{km s}^{-1} \text{ kpc}^{-1}$ .

<sup>c</sup> In units of  $\text{km s}^{-1} \text{ kpc}^{-1} (M_\odot \text{ pc}^{-2})^{-1}$ .

however, is lower than in the other regions. The lower value for interarm 1 can be inferred directly from the profile itself (Fig. 15). The tangential velocities in both arms are clearly rising, and  $v_\theta$  in interarm 2 (downstream from arm 2 at  $\psi = 200^\circ$ ) is predominantly decreasing, suggesting that the spiral arms have the most significant influence on the velocities in these regions. In interarm 1 (downstream from arm 1 at  $\psi = 0^\circ$ ), however, there is more structure to the velocities, suggesting that there are other sources of perturbations in addition to the spiral arms. We find that for most of the velocity profiles in Figure 14 and 15 the vortensity values are consistent between the two arms, within the errors. However, in the interarms the vortensity values differ. We find varying vortensity values in all interarm regions except for interarm 2 indicated in Table 3. Overall, the agreement between vortensity in arm regions in each annulus indicates either that a steady state depiction of the vortensity is valid and there is very little radial migration of gas, or else that in a given annulus much of the gas originated in a region of constant vortensity and has been conserved along streamlines as gas in a whole annulus flows inward or outward.

## 6.2. Conservation of Mass

### 6.2.1. Flux-Weighted Average $v_R$

In the QSSS scenario, the spiral pattern—as defined by its amplitude, phase, and rotation rate—would not change significantly over the course of a few revolutions in a frame rotating along with the spiral pattern (Lindblad 1963; Bertin & Lin 1996). Such a framework suggests that on average any accretion of material into the arms should be balanced by the same amount of material exiting downstream. This condition corresponds to conservation of mass for a steady state system; if this condition holds it should be apparent in the variation of observed velocities with spiral-arm phase.

As can be seen in Figures 14 and 15, the spiral arms clearly perturb  $v_\theta$  with deviations of  $\geq 100 \text{ km s}^{-1}$  but  $v_\theta$  always remains positive, indicating that the orbital flow is in one direction only. However, the radial velocities do change sign, indicating both inflow and outflow. If the spiral arms are indeed a quasi-stationary pattern, then large amounts of matter should not be undergoing net inflow or outflow; i.e., the mass-weighted average radial velocity cannot be too large. A large or spatially strongly variable mass-weighted average  $v_R$  would imply a very dynamic system. In particular, if the sign of this quantity changes, then there would be a buildup or depletion of mass in one or more radial locations.

As discussed in § 4.3, the fit for  $v_R$  is very sensitive to the assumed value of the position angle. Thus, in investigating the mass-weighted average radial velocity, we consider a range of position angles. Figure 17 shows the  $v_R$  fits for H $\alpha$  in annuli with radii of  $47''\text{--}80''$  and  $61''\text{--}105''$  for three different position angles,  $170^\circ$ ,  $175^\circ$ , and  $180^\circ$ . The CO fits are similar but noisier and have larger error bars (see Figs. 14–15). A striking aspect of the fits in Figure 17 is the large magnitude of inflow in the arms for all three position angles; the radial velocity drops to as low as  $-75 \text{ km s}^{-1}$ , suggesting significant inflow for gas in the spiral arms. In the upstream regions  $v_R$  is positive, approaching  $70 \text{ km s}^{-1}$  for some parameter choices. For a region farther in, in the  $27''\text{--}47''$  annulus shown in Figures 14 and 15, the fitted radial velocity (assuming  $\theta_{MA} = 170^\circ$ ) reaches values greater than  $100 \text{ km s}^{-1}$ , indicating tremendous outflow in the inner regions; assuming a position angle of  $180^\circ$  for this annulus only reduces the peak velocity from  $\approx 100 \text{ km s}^{-1}$  to  $\approx 75 \text{ km s}^{-1}$ .

Figure 18 shows the flux-weighted average radial velocity ( $\langle v_R \rangle$ ) for different position angles in the different annuli used in

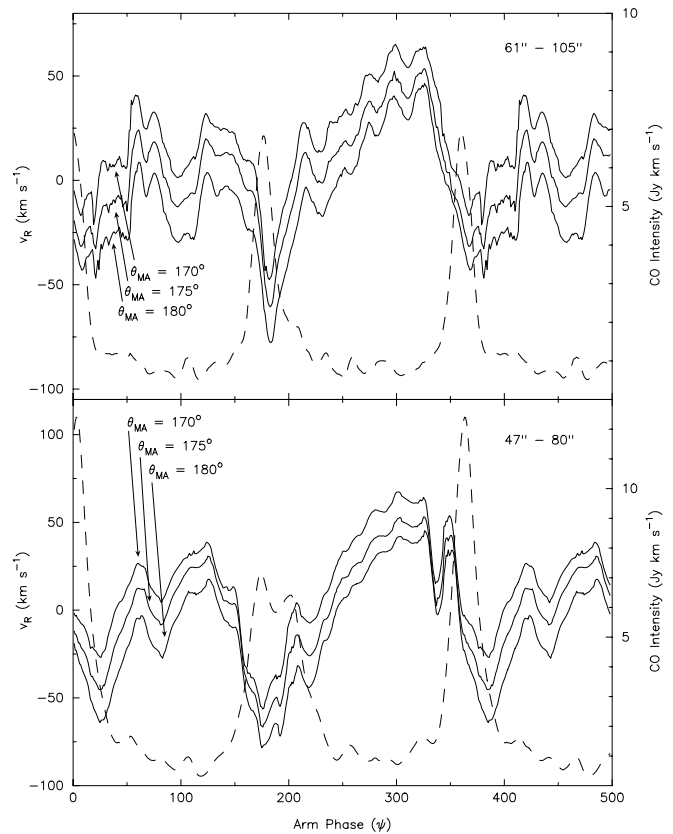


FIG. 17.—H $\alpha$   $v_R$  fits as a function of arm phase for three different position angles  $\theta_{MA}$ ,  $170^\circ$ ,  $175^\circ$ , and  $180^\circ$ , for two annuli ( $47''\text{--}80''$  and  $61''\text{--}105''$ ). We fix the inclination at  $24^\circ$ , and other parameters used in the fitting are shown in Table 1. The dashed line is the mean CO intensity along the arm for a  $\theta_{MA}$  of  $170^\circ$ , which varies only slightly with  $\theta_{MA}$ . The error bars are not shown because they are similar to those shown in Fig. 15.

the fitting process. With the canonical position angle of  $170^\circ$ , there is significant outflow in the inner regions of M51. On the other hand, a position angle of  $180^\circ$  seems appropriate for the innermost regions of M51, since this yields a lower value of  $\langle v_R \rangle$ . However, with such a position angle we find significant inflow in the outer region. If we adopt an intermediate position angle of  $175^\circ$ , there is outflow in the inner regions and inflow in the outer regions. For a  $\theta_{MA}$  of  $175^\circ$ ,  $\langle v_R \rangle = 0$  for the  $36''\text{--}61''$  annulus, with mean radius  $\langle R \rangle = 1.98 \text{ kpc}$ , while adjacent annuli have  $\langle v_R \rangle = 10$  and  $-20 \text{ km s}^{-1}$  for  $\langle R \rangle = 1.5$  and  $2.6 \text{ kpc}$ , respectively ( $1'' = 40.7 \text{ pc}$  at a distance of  $8.4 \text{ Mpc}$ ). If this were true, then the gas would all collect near  $R \approx 2 \text{ kpc}$  in less than one orbital timescale ( $\sim 200 \text{ Myr}$ ), which is not consistent with a steady state.

This analysis leads us to conclude that if the spiral pattern is long lived, the large variations in the radial velocity shown in Figure 18 suggests that the position angle must vary with radius, indicating a disk that is not coplanar. This trend suggesting a larger position angle in the inner regions and a smaller position angle in the outer regions is also in accordance with the position angle tests described in § 4.3 (see Fig. 13).

We schematically show a disk with a varying position in Figure 19; the position angles of the ellipses are arranged as indicated by Figure 13. As discussed, one effect of a variation of position angle is a disk that is not coplanar. The inclination in this schematic is exaggerated; the observed morphology, including the apparent spiral structure, depends on the viewing angle, among other factors.

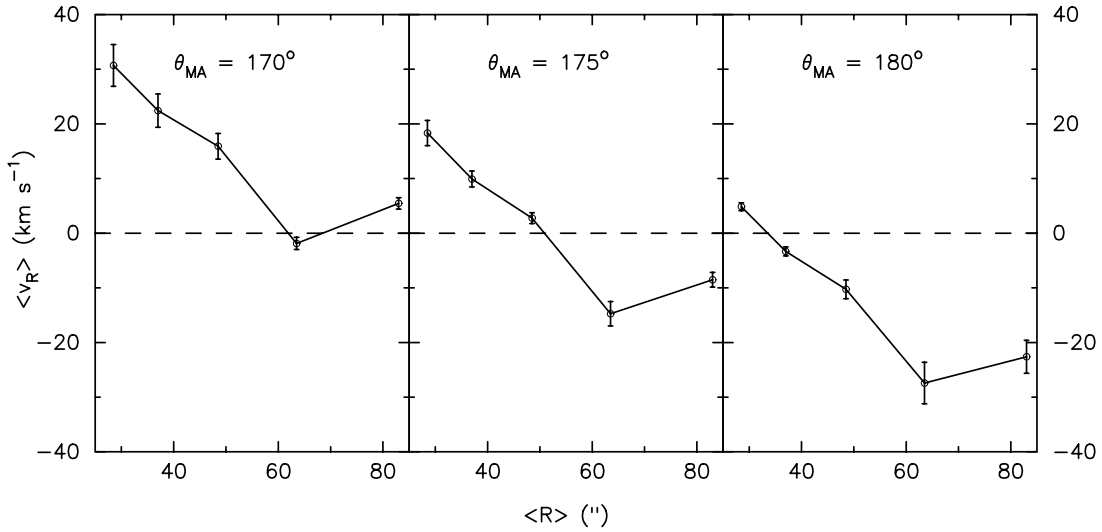


FIG. 18.—Mass-weighted average radial velocities  $\langle v_R \rangle$  in the different annuli, two of which are shown in Fig. 17. The abscissa indicates the mean radius  $\langle R \rangle$ , in arcseconds, of each annulus. The three panels show the mass-weighted average  $v_R$  assuming three different values for the position angle  $\theta_{MA}$ . The error bars include both fitted errors in  $v_R$  (see Fig. 14) and an estimated error of 20% in  $\Sigma$ .

6.2.2. Continuity and Spiral Pattern Speed

In this section we explore the plausibility of QSSS using the gas continuity equation. The continuity equation for gas flow in a two-dimensional system is

$$\frac{\partial \Sigma}{\partial t} + \nabla \cdot (\Sigma \mathbf{v}) = 0; \tag{14}$$

this holds in any frame, e.g., whether the velocity is measured in an inertial frame or one rotating at a constant pattern speed. The first term,  $\partial \Sigma / \partial t$ , represents the temporal growth or decay of the surface density  $\Sigma$  at any given radius  $R$  and azimuthal angle  $\theta$  in the plane of the galaxy, where those coordinates are with respect to the frame in which the velocity is being measured.

If the flow is in a steady state, then the temporal term vanishes, leaving only the mass flux term  $\Sigma \mathbf{v}$ . If the gas is responding primarily to a single dominant spiral perturbation, as would be required for a fixed spiral pattern, and when  $\mathbf{v}$  is measured in the frame rotating at the pattern angular velocity  $\Omega_p$ ,

$$\nabla \cdot [\Sigma (\mathbf{v}_{\text{inertial}} - \Omega_p R \hat{\theta})] = 0. \tag{15}$$

Thus, for an exact steady state the mass flux must be constant (in the frame rotating with the same angular velocity as the spiral mode). For a quasi-steady state, the temporal variations in  $\Sigma$  will only be small, and thus variations in mass flux would also

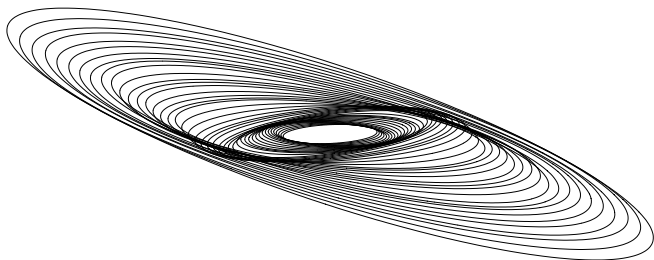


FIG. 19.—Model disk showing the variation of the position angle with radius. The position angle profile is taken from Fig. 13. The inclination is exaggerated to show a more edge-on view.

be small. This condition can be further simplified using a reference frame aligned locally with the spiral arms. Figure 20 shows this reference frame; the  $x$  and  $y$  coordinates are the directions perpendicular and parallel to the local spiral arm, respectively. The transformation between cylindrical coordinates and this arm frame is achieved using

$$\hat{x} = \cos i_p \hat{R} + \sin i_p \hat{\theta}, \tag{16}$$

$$\hat{y} = -\sin i_p \hat{R} + \cos i_p \hat{\theta}, \tag{17}$$

where  $i_p$  is the pitch angle of the arms.

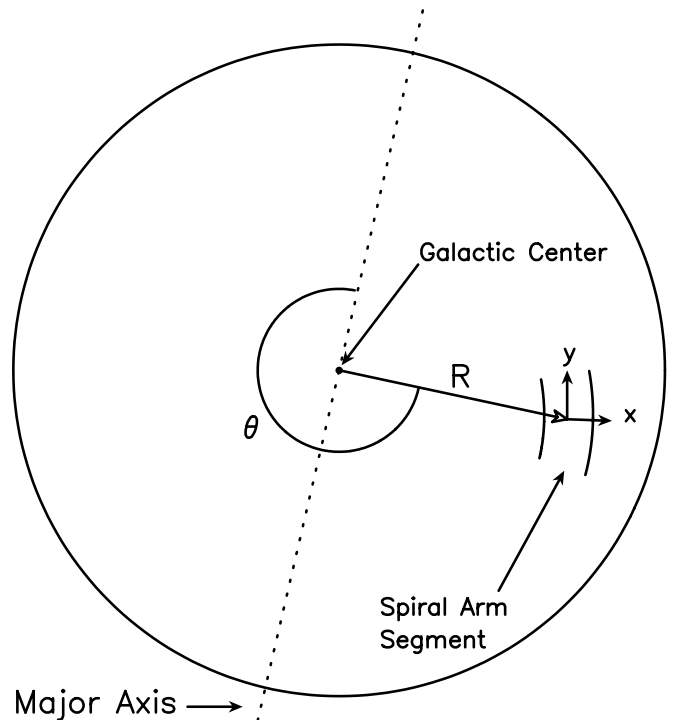


FIG. 20.—Coordinate transformation geometry, from  $(R, \theta)$  galactocentric coordinates to the  $(x, y)$  spiral-arm frame.

TABLE 4  
MASS FLUX IN THE 47''–80'' ANNULUS

Region	$\Sigma^a$	$v_R \cos i_p^b$	$(v_\theta - \Omega_p R) \sin i_p^b$	$C^c$	$\Sigma \tilde{v}_x^d$
$\theta_{MA} = 170^\circ$ :					
Arm 1 ( $\psi \approx 360^\circ$ ).....	244	–24	41	$-58 \pm 30$	–10113
Arm 2 ( $\psi \approx 190^\circ$ ).....	128	–53	32	$-58 \pm 30$	–10113
Interarm 1 ( $\psi \approx 90^\circ$ ).....	16	23	18	...	–259
Interarm 2 ( $\psi \approx 275^\circ$ ).....	19	49	21	...	237
$\theta_{MA} = 175^\circ$ :					
Arm 1 ( $\psi \approx 360^\circ$ ).....	244	–41	41	$-32 \pm 18$	–8103
Arm 2 ( $\psi \approx 190^\circ$ ).....	128	–63	32	$-32 \pm 18$	–8103
Interarm 1 ( $\psi \approx 90^\circ$ ).....	16	12	18	...	–38
Interarm 2 ( $\psi \approx 275^\circ$ ).....	19	36	21	...	464
$\theta_{MA} = 180^\circ$ :					
Arm 1 ( $\psi \approx 360^\circ$ ).....	244	–59	41	$-8 \pm 17$	–6345
Arm 2 ( $\psi \approx 190^\circ$ ).....	128	–71	32	$-8 \pm 17$	–6345
Interarm 1 ( $\psi \approx 90^\circ$ ).....	16	1	18	...	182
Interarm 2 ( $\psi \approx 275^\circ$ ).....	19	27	21	...	761

<sup>a</sup> In units of  $M_\odot \text{pc}^{-2}$ ; error of  $\sim 20\%$ .

<sup>b</sup> In units of  $\text{km s}^{-1}$ .

<sup>c</sup> In units of  $\text{km s}^{-1}$ ; error largely due to errors in  $\Sigma$  and  $\Omega_p$ .

<sup>d</sup> In units of  $M_\odot \text{pc}^{-2} \text{km s}^{-1}$ .

The velocities in the arm frame are given by

$$v_x = v_R \cos i_p + (v_\theta - \Omega_p R) \sin i_p, \quad (18)$$

$$v_y = -v_R \sin i_p + (v_\theta - \Omega_p R) \cos i_p. \quad (19)$$

From the maps shown in Figures 1 and 4, it is apparent that the intensity and velocity vary significantly more across the arms, in the  $x$ -direction, than along them, in the  $y$ -direction. Thus, the variation in the product of  $\Sigma v_y$  along  $\hat{y}$  is much smaller than the variation in the product of  $\Sigma v_x$  along  $\hat{x}$ , reducing equation (15) to

$$\Sigma v_x \approx \text{constant}. \quad (20)$$

Namely, for a steady pattern, as the gas decelerates (in the  $x$ -direction, perpendicular to the arm), mass accumulates and the surface density increases; as the gas velocity increases, the surface density decreases.

One difficulty in testing whether equation (20) holds is that neither  $\theta_{MA}$  nor  $\Omega_p$  is well constrained. Errors in  $\theta_{MA}$  yield errors in the fitted value of  $v_\theta$  of  $\approx v_R \sin \Delta\theta_{MA}$  and in the fitted value of  $v_R$  of  $\approx -v_\theta \sin \Delta\theta_{MA}$ . If  $\Delta\Omega_p$  is the error in the pattern speed, then the fitted value of  $v_x$  will be approximately given by  $v_x + (-v_\theta \sin \Delta\theta_{MA} \cos i_p + v_R \sin \Delta\theta_{MA} \sin i_p - \Delta\Omega_p R \sin i_p)$ . Since the  $v_R$  term has two factors of the  $\sin$  of small angles, that term will be much smaller compared with the other two terms. The true value of  $v_x$  will therefore differ from the fitted value by  $C_x \approx v_\theta \sin \Delta\theta_{MA} \cos i_p + \Delta\Omega_p R \sin i_p$ .

In order to assess whether steady state continuity as expressed by equation (20) holds in the case of M51, we therefore consider the quantity

$$\Sigma \tilde{v}_x = \Sigma [v_R \cos i_p + (v_\theta - \Omega_p R) \sin i_p + C], \quad (21)$$

where  $v_R$  and  $v_\theta$  are fitted values and  $C \equiv \langle C_x \rangle$ , i.e., the (unknown) azimuthally averaged correction due to the errors in  $\theta_{MA}$  and  $\Omega_p$ .

We apply equation (21) by solving for the value of  $C$  using the values of  $v_R$ ,  $v_\theta$ , and  $\Sigma$  in the two arm segments of an annulus:

$$C = \{ [v_{R, \text{arm1}} \cos i_p + (v_{\theta, \text{arm1}} - \Omega_p R) \sin i_p] \Sigma_{\text{arm1}} - [v_{R, \text{arm2}} \cos i_p + (v_{\theta, \text{arm2}} - \Omega_p R) \sin i_p] \Sigma_{\text{arm2}} \} \times (\Sigma_{\text{arm2}} - \Sigma_{\text{arm1}})^{-1}. \quad (22)$$

We then test whether the value of  $C$  obtained using equation (22) also satisfies equation (21) in the interarm regions. If equation (21) is satisfied for both interarm and arm regions, it would suggest an approximate steady state.

We again focus on the 47''–80'' annulus, where the  $v_R$  (and  $v_\theta$ ) are relatively ‘‘smooth.’’ The  $v_R$  profiles for this annulus is shown in Figure 17, assuming three different values of the position angle. Table 4 shows the relevant values associated with equation (21) for the arms and interarm regions. We employ the pattern speed of  $38 \pm 7 \text{ km s}^{-1} \text{ kpc}^{-1}$ , calculated by Zimmer et al. (2004) by applying the Tremaine-Weinberg method to CO observations of M51. Corotation corresponding to this pattern speed is marked on Figure 16. After solving for  $C$  using quantities from the arms, it is clear that the flow in the interarm region is not consistent with a steady state description. A position angle of  $170^\circ$  produces large negative mass flux in the arms, and positive flux in one interarm region. Even variations in the  $X$ -factor cannot resolve this discrepancy. Assuming larger values of the position angle still produces mass fluxes with vastly different magnitudes, and even different signs. Increasing the error in  $C$  up to an order of magnitude still cannot result in consistent mass fluxes between the arm and interarm. This suggests that any reasonable changes to the values of  $\theta_{MA}$  or  $\Omega_p$  will still result in varying mass fluxes. We have checked the mass flux in other annuli using the same method as for the 47''–80'' annulus, as well as in other localized regions not presented here, and found similar discrepancies in the mass flux.

In our analysis of continuity so far, we have not taken into account the contribution from the atomic component of the disk. In fact, in most galaxies the majority of the gas exists in the form of H I. In M51, Tilanus & Allen (1989) showed that the downstream offset of H I relative to the dust lanes is likely due to

dissociation of molecular gas by recently formed massive stars. However, the inner disk of M51 has an unusually large fraction of molecular gas, so even at peaks of the H I photodissociation arms, the contribution of atomic gas to the total gas surface density is negligible. Using the H I maps of Rots et al. (1990) we find that the atomic column density  $N(\text{H I})$  is significantly less than the molecular column density  $N(\text{H}_2)$  in the vast majority of locations in the inner disk ( $21'' \leq R \leq 105''$ );  $N(\text{H I})$  exceeds  $N(\text{H}_2)$  in only  $\sim 7\%$  of the inner disk. The mean value of  $N(\text{H}_2)/N(\text{H I})$  throughout the inner region is  $\sim 10$ . Although we used a constant X-factor to obtain the molecular surface density, moderate variations in the X-factor (for M51, see Nakai & Kuno 1995) will not be sufficient to account for the discrepancy. Nevertheless, no change in the X-factor, or in the contributions of the molecular or atomic matter to the total mass, can account for the change in sign of the mass flux; the varying sign of  $\Sigma v_x$  can only be due to a sign change in  $v_x$ , not  $\Sigma$ .

Our conclusion, after analyzing the mass flux, is that the kinematics are not consistent with a quasi-steady spiral pattern in a flat disk. We find that no single pattern speed can satisfy quasi-steady state continuity, suggesting that the QSSS hypothesis is not applicable to M51. It is essentially the tremendous variations of the radial velocity within a given annulus—amounting to  $\sim 100 \text{ km s}^{-1}$ —that lead the QSSS hypothesis into difficulty. One explanation for the transient nature of the spiral arms in M51, perhaps due to the interaction with its companion, is a spiral perturbation with a constant pattern speed, but with time-varying amplitude. Or, there may be multiple modes at work in the disk of M51, which may be construed as a mode with a radially varying pattern speed (e.g., Merrifield et al. 2006). Multiple pattern speeds in M51 have been previously suggested by Vogel et al. (1993) and Elmegreen et al. (1989). However, the extreme variations in the radial velocity cannot be explained by multiple patterns alone. Possible causes for the large observed  $v_R$  gradients are large out-of-plane motions or a variation in inclination; since the inclination of M51 is small, a variation in  $i$  due to a warped or twisted disk will produce large variations in the observed velocity due to projection effects.

### 6.3. Discussion

We have shown that the density and velocity structure in M51 does not support a quasi-steady state depiction for the spiral pattern, using measurements of the mass flux. Further evidence that the observed structure is inconsistent with steady state can be obtained by adopting the fitted 2D velocity field, and demonstrating that the density structure is then nonsteady. We have carried out this exercise using a modified version of the NEMO task `flowcode` (Teuben 1995). In this exercise, a disk is populated with gas tracer particles using the intensity profiles averaged along spiral segments, reproducing the spiral density pattern of M51. Each location in the disk has an associated  $v_R$  and  $v_\theta$ , given by the fitted velocity profiles (e.g., Figs. 14 and 15), and an assumed value of the pattern speed. The motion of the particles is then integrated using `flowcode`: after a suitably small time step, the particles take on new velocities depending on their location in the disk. In essence, this simulation is a purely kinematic test to determine whether the steady state continuity equation (eq. [15]) is satisfied or not, using the density and fitted velocity profiles of M51 (Figs. 14 and 15). We find that the input spiral pattern vanishes in less than one orbital timescale ( $\sim 200 \text{ Myr}$ ), regardless of what values of the position angle and pattern speed we assume.

The precise nature of the velocities is one of a number of issues that need to be considered in further studying the global spiral pattern in M51. For example, our result suggests the role of a warp certainly needs to be taken into account. There are strong indications that the outer disk of M51 is warped; our finding suggests that the disk is not coplanar even further inward. The non-coplanar attribute may be the result of the tidal interaction between M51 and its companion.

The possible warp and/or twist in the disk of M51 would of course affect the projected velocities, and would present itself as gradients in the velocity components, as discussed in the previous section. If this were indeed the case, then the single or multiple in-plane modes would have to be in phase with the vertical mode in order to sustain a spiral pattern. The inherent uncertainty in deriving three velocity components from the single observed component leads to difficulty in estimating and analyzing both the vertical and in-plane modes.

## 7. SUMMARY

We have analyzed the velocity field of M51, using CO and H $\alpha$  observations, to investigate the nature of the spiral structure. We summarize the main results here:

1. The velocity field is quite complex. Observed velocities show significant azimuthal streaming associated with the spiral arms, as well as strong gradients in the radial velocities.
2. The aberrations in the velocity field strongly suggest that the disk is not coplanar, perhaps as far in as  $20''$  ( $\sim 800 \text{ pc}$ ) from the center.
3. We obtain fitted radial and tangential velocity profiles by assuming that velocities in any annulus vary only with arm phase. Strong gradients in the radial and tangential velocities are found in the profile fits. In general, the shapes of both the  $v_R$  and  $v_\theta$  profiles are in qualitative agreement with theory of nonlinear density waves, and support the presence of shocks.
4. In detail, the velocity profiles from different radial regions of M51 differ significantly. In addition, velocity profiles associated with the two arms also show differences in a given annulus. For the arm that is well described by a logarithmic spiral (bright arm), the associated velocities are in good agreement with simple theoretical spiral shock profiles. For the other arm, which is not as well described by a logarithmic spiral, the velocities are more complex.
5. The velocity profile fits from CO and H $\alpha$  emission are rather similar, suggesting that most of the H $\alpha$  emission originates from gas associated with star-forming regions.
6. When we assume single values for the inclination and position angle of the major axis, we find that large amounts of material flows toward an annulus of intermediate radius, due to the large gradients and change of sign in the flux-weighted average radial velocity. As a result, either the position angle of the major axis or the inclination must vary with radius, suggesting that the disk of M51 is warped and twisted.
7. We analyze conservation of vortensity, using the radial and tangential velocity profile fits. We find that vortensity is fairly consistent within a given annulus, indicating that the gas there all originated in a region of uniform vortensity.
8. Using the equation of continuity, we find that the density and fitted velocity profiles are inconsistent with quasi-steady state mass conservation in any frame rotating at a constant angular speed, at least for a planar system. Variations in the pattern speed, position angle, and X-factor alone cannot account for the differences in the mass flux, suggesting that spiral arms are quite dynamic, and possibly that out-of-plane motions are significant.

We are grateful to S. McGaugh for his help in using the baryonic Tully-Fisher relation to estimate the inclination of M51. We thank W. T. Kim for useful discussions, and G. Gómez for providing velocity profiles from his hydrodynamic models. We also

thank the anonymous referee for raising many interesting questions and useful suggestions. This research was supported in part by grants AST 02-28974 and AST 05-07315 from the National Science Foundation.

## REFERENCES

- Aalto, S., Hüttmeister, S., Scoville, N. Z., & Thaddeus, P. 1999, *ApJ*, 522, 165  
 Begeman, K. G. 1989, *A&A*, 223, 47  
 Bell, E. F., & de Jong, R. S. 2001, *ApJ*, 550, 212  
 Bertin, G., & Lin, C. C. 1996, *Spiral Structure in Galaxies: A Density Wave Theory* (Cambridge: MIT Press)  
 Bertin, G., Lin, C. C., Lowe, S. A., & Thurstans, R. P. 1989a, *ApJ*, 338, 78  
 ———. 1989b, *ApJ*, 338, 104  
 Calzetti, D., et al. 2005, *ApJ*, 633, 871  
 Charlot, S., & Bruzual A., G. 1991, *ApJ*, 367, 126  
 de Vaucouleurs, G., de Vaucouleurs, A., Corwin, Jr., H. G., Buta, R. J., Paturel, G., & Fouqué, P. 1991, *Third Reference Catalogue of Bright Galaxies* (Berlin: Springer)  
 Elmegreen, B. G., Seiden, P. E., & Elmegreen, D. M. 1989, *ApJ*, 343, 602  
 Elmegreen, D. M. 1980, *ApJ*, 242, 528  
 Feldmeier, J. J., Ciardullo, R., & Jacoby, G. H. 1997, *ApJ*, 479, 231  
 Gittins, D. M., & Clarke, C. J. 2004, *MNRAS*, 349, 909  
 Gómez, G. C., & Cox, D. P. 2002, *ApJ*, 580, 235  
 Gruendl, R. A. 1996, Ph.D. thesis, Univ. Maryland  
 Hagiwara, Y., Henkel, C., Menten, K. M., & Nakai, N. 2001, *ApJ*, 560, L37  
 Helfer, T. T., Thornley, M. D., Regan, M. W., Wong, T., Sheth, K., Vogel, S. N., Blitz, L., & Bock, D. C.-J. 2003, *ApJS*, 145, 259  
 Henry, A. L., Quillen, A. C., & Gutermuth, R. 2003, *AJ*, 126, 2831  
 Ho, P. T. P., Martin, R. N., Henkel, C., & Turner, J. L. 1987, *ApJ*, 320, 663  
 Jensen, J. B., Tonry, J. L., & Luppino, G. A. 1996, *BAAS*, 28, 1419  
 Kennicutt, R. C., Jr., et al. 2003, *PASP*, 115, 928  
 Kim, W.-T., & Ostriker, E. C. 2002, *ApJ*, 570, 132  
 Kuno, N., & Nakai, N. 1997, *PASJ*, 49, 279  
 La Vigne, M. A., Vogel, S. N., & Ostriker, E. C. 2006, *ApJ*, 650, 818  
 Lin, C. C., & Shu, F. H. 1964, *ApJ*, 140, 646  
 Lindblad, B. 1963, *Stockholm Obs. Ann.*, 22(5), 1  
 Lowe, S. A., Roberts, W. W., Yang, J., Bertin, G., & Lin, C. C. 1994, *ApJ*, 427, 184  
 Lubow, S. H., Cowie, L. L., & Balbus, S. A. 1986, *ApJ*, 309, 496  
 McGaugh, S. S. 2005, *ApJ*, 632, 859  
 McGaugh, S. S., Schombert, J. M., Bothun, G. D., & de Blok, W. J. G. 2000, *ApJ*, 533, L99  
 Merrifield, M. R., Rand, R. J., & Meidt, S. E. 2006, *MNRAS*, 366, L17  
 Nakai, N., & Kasuga, T. 1988, *PASJ*, 40, 139  
 Nakai, N., & Kuno, N. 1995, *PASJ*, 47, 761  
 Rand, R. J. 1993, *ApJ*, 410, 68  
 Regan, M. W., Thornley, M. D., Helfer, T. T., Sheth, K., Wong, T., Vogel, S. N., Blitz, L., & Bock, D. C.-J. 2001, *ApJ*, 561, 218  
 Rix, H.-W., & Rieke, M. J. 1993, *ApJ*, 418, 123  
 Roberts, W. W. 1969, *ApJ*, 158, 123  
 Roberts, W. W., & Stewart, G. R. 1987, *ApJ*, 314, 10  
 Rots, A. H., Bosma, A., van der Hulst, J. M., Athanassoula, E., & Crane, P. C. 1990, *AJ*, 100, 387  
 Salo, H., & Laurikainen, E. 2000, *MNRAS*, 319, 377  
 Shetty, R., & Ostriker, E. C. 2006, *ApJ*, 647, 997  
 Shu, F. H., Milione, V., & Roberts, W. W., Jr. 1973, *ApJ*, 183, 819  
 Strong, A. W., et al. 1988, *A&A*, 207, 1  
 Teuben, P. 1995, in *ASP Conf. Ser. 77, Astronomical Data Analysis Software and Systems IV*, ed. R. A. Shaw, H. E. Payne, & J. J. E. Hayes (San Francisco: ASP), 398  
 Tilanus, R. P. J., & Allen, R. J. 1989, *ApJ*, 339, L57  
 Toomre, A., & Toomre, J. 1972, *ApJ*, 178, 623  
 Tully, R. B. 1974, *ApJS*, 27, 449  
 Tully, R. B., & Fisher, J. R. 1977, *A&A*, 54, 661  
 van der Kruit, P. C., & Shostak, G. S. 1982, *A&A*, 105, 351  
 Verheijen, M. A. W. 2001, *ApJ*, 563, 694  
 Visser, H. C. D. 1980, *A&A*, 88, 149  
 Vogel, S. N., Kulkarni, S. R., & Scoville, N. Z. 1988, *Nature*, 334, 402  
 Vogel, S. N., Rand, R. J., Gruendl, R. A., & Teuben, P. J. 1993, *PASP*, 105, 666  
 Woodward, P. R. 1975, *ApJ*, 195, 61  
 Zimmer, P., Rand, R. J., & McGraw, J. T. 2004, *ApJ*, 607, 285